

Applying Astronomical Solutions and Milanković Forcing in the Earth Sciences

Richard E. Zeebe^{1,*} and Ilja J. Kocken¹

*Corresponding Author.

¹School of Ocean and Earth Science and Technology, University of Hawaii at Manoa, 1000 Pope Road, MSB, Honolulu, HI 96822, USA. zeebe@soest.hawaii.edu, ikocken@hawaii.edu

[0000 – 0003 – 0806 – 8387] Richard E. Zeebe
[0000 – 0003 – 2196 – 8718] Ilja J. Kocken

Final revised version in press. October 18, 2024

Contents

1	Introduction	2
1.1	The Main Milanković Cycles	7
1.2	Types of Astronomical Solutions	8
1.3	Organization of Content	9
2	Orbital Solutions	9
2.1	Fundamentals	9
2.1.1	Orbital Elements	9
2.1.2	Eccentricity and Inclination	11
2.1.3	Secular Frequencies: g and s Modes	12
2.1.4	Frequency Combination Terms: Eccentricity & Obliquity-Modulation	16
2.2	The so-called “Metronomes”	17
2.3	Solar System Chaos	18
2.3.1	The Driven Pendulum: Poincaré Section	18
2.3.2	Solar System: Time Scales and Limitations	21
2.3.3	Divergence Time τ	23
2.3.4	Chaos and Inapplicability of Basic Statistics	23
2.4	Amplitude & Frequency Modulation (AM & FM)	24
2.4.1	AM	25
2.4.2	FM	26
2.5	Up-to-Date Orbital Solutions	27
2.6	Additional Physical/Dynamical Effects in Up-to-Date Orbital Solutions	29
3	Precession-Tilt Solutions	29
3.1	Luni-Solar and Climatic Precession	30
3.2	Luni-Solar (Equatorial) and Planetary (Ecliptic) Precession	32
3.2.1	Luni-Solar Precession: Long-term Variations	34
3.3	Dynamical Ellipticity and Tidal Dissipation	35
3.4	Up-to-date Precession and Obliquity Solutions	36
3.5	Milanković Forcing in Deep Time	37
4	Practical Considerations	39
4.1	Available Resources	39
5	Summary & Outlook	40
Appendix A	Precession Equations	42

Abstract

Astronomical solutions provide calculated orbital and rotational parameters of solar system bodies based on the dynamics and physics of the solar system. Application of astronomical solutions in the Earth sciences has revolutionized our understanding in at least two areas of active research. (i) The Astronomical (or Milanković) forcing of climate on time scales $\gtrsim 10$ kyr and (ii) the dating of geologic archives. The latter has permitted the development of the astronomical time scale, widely used today to reconstruct highly accurate geological dates and chronologies. The tasks of computing vs. applying astronomical solutions are usually performed by investigators from different backgrounds, which has led to confusion and recent inaccurate results on the side of the applications. Here we review astronomical solutions and Milanković forcing in the Earth sciences, primarily aiming at clarifying the astronomical basis, applicability, and limitations of the solutions. We provide a summary of current up-to-date and outdated astronomical solutions and their valid time span. We discuss the fundamental limits imposed by dynamical solar system chaos on astronomical calculations and geological/astrochronological applications. We illustrate basic features of chaotic behavior using a simple mechanical system, i.e., the driven pendulum. Regarding so-called astronomical “metronomes”, we point out that the current evidence does not support the notion of generally stable and prominent metronomes for universal use in astrochronology and cyclostratigraphy. We also describe amplitude and frequency modulation of astronomical forcing signals and the relation to their expression in cyclostratigraphic sequences. Furthermore, the various quantities and terminology associated with Earth’s axial precession are discussed in detail. Finally, we provide some suggestions regarding practical considerations.

Keywords:

Astronomical Forcing, Milanković Theory, Paleoclimatology, Astrochronology, Cyclostratigraphy, Solar System, Orbital dynamics, Planetary climate

1. Introduction

The term “astronomical solution” (\mathcal{AS}) as used here refers to calculated planetary orbital and rotational parameters over time based on known solar system physics at a specified point in time. Mathematically, an \mathcal{AS} for the planetary orbits represents a solution to the equations of motion of the solar system with initial conditions at time t_0 for the positions, velocities, and masses of the solar system bodies included in the calculation. Here we will focus specifically on \mathcal{AS} s that have direct applications in the Earth sciences, for instance, in geology, paleoclimatology, astrochronology, and cyclostratigraphy; i.e., \mathcal{AS} s that provide accurate values for Earth’s orbital parameters in the past (for a specific example, see Fig. 1). Thus, while a general review of \mathcal{AS} s may start historically with the work of Johannes Kepler,

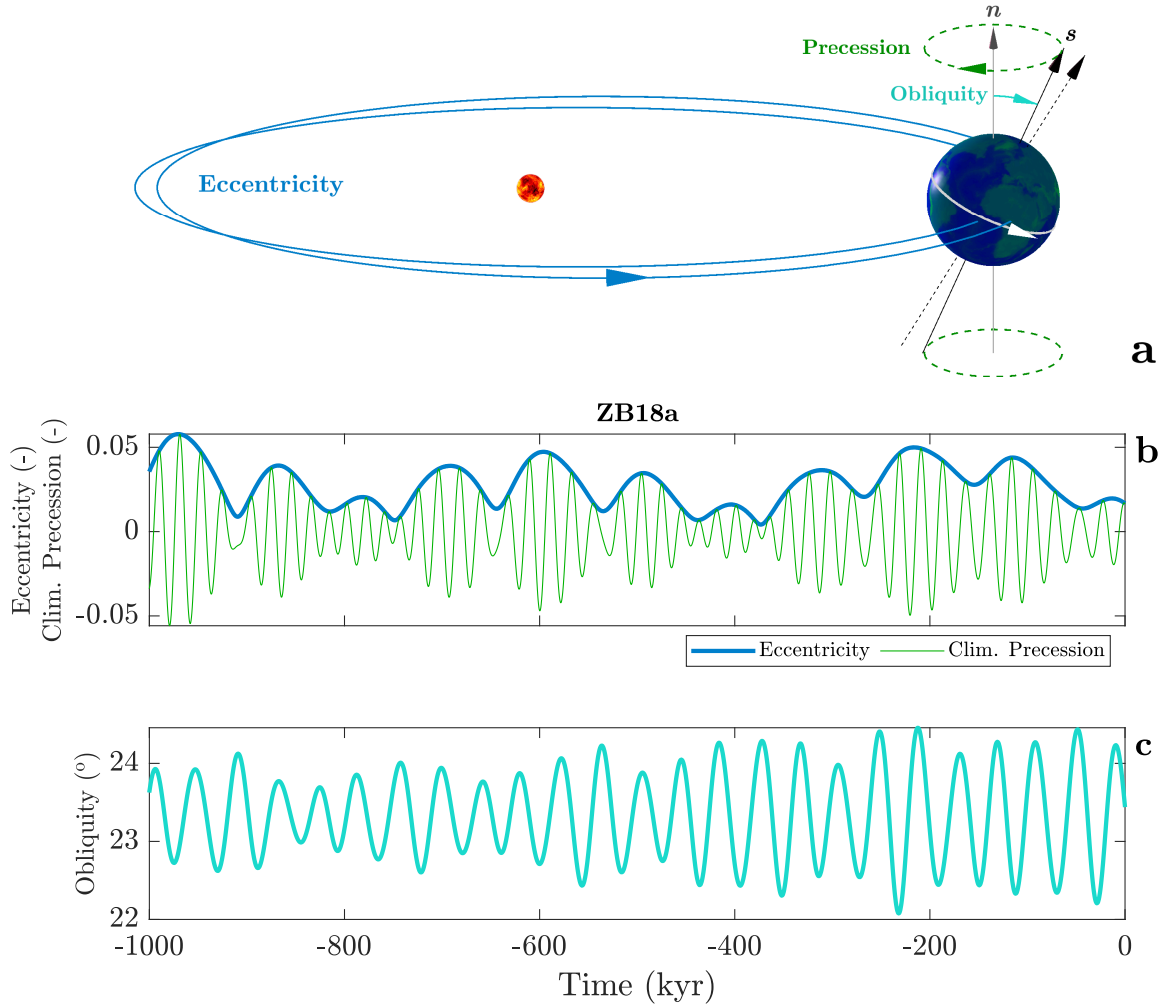


Figure 1: Example of orbital parameters and their values frequently used in the Earth sciences. (a) Illustration of orbital eccentricity (recent main periods ~ 100 and 405 kyr), precession (~ 20 kyr), and obliquity (~ 41 kyr), often called Milanković cycles (for geometrical illustrations of their physical meaning, see also Figs. 2 and 14). For illustration, Earth’s orbital eccentricity is highly exaggerated. For an elliptical orbit, the sun is located at one of the ellipses’ foci. Obliquity is the angle between Earth’s spin axis (spin vector \mathbf{s}) and the orbit normal (unit vector \mathbf{n} perpendicular to Earth’s orbital plane = ecliptic, see Table 1). Viewed from ecliptic north, Earth’s rotation (spin) is counterclockwise (from west-to-east, or eastward). Earth’s orbital motion is in the same direction (prograde). Axial precession (precession of the equinoxes) is in the opposite direction (retrograde, green arrow). Orbital parameter values shown here are from/based on the orbital solution ZB18a (Zeebe and Lourens, 2019, 2022a) over the past 1 Myr. (b) Earth’s orbital eccentricity (blue) from ZB18a and climatic precession (green) based on ZB18a. (c) Obliquity of Earth’s spin axis based on ZB18a.

we start with the work of Milutin Milanković, a Serbian engineer and mathematician (1879–1958).

Although not the first to propose astronomically-driven climate change on Earth (for a review, see Emiliani, 1995), Milanković worked out an astronomical theory to calculate the effects of secular (‘slow’) changes in insolation on Earth’s climate and was primarily interested in applying the astronomical theory to the ice age problem. In 1941, Milanković summarized his findings spanning thirty years of work in a 633-page volume to the Serbian Royal Academy (Milanković, 1941). Milanković used an \mathcal{AS} that included elements of Leverrier’s work and contributions from Mišković (see Milanković, 1941, p. 335 ff.). Notably, Milanković’s astronomical theory of paleoclimate was far from accepted at the time and was virtually ignored for decades before being recognized by a larger community that realized its merit (e.g., Emiliani, 1955; Broecker, 1966; Imbrie and Kipp, 1971; Hays et al., 1976; Berger, 1978). Today, there is overwhelming evidence that Earth’s climate is paced by astronomical cycles on time

Table 1: Notation and values employed in this paper (frequently used variables).

Symbol	Meaning	Value I/A	Unit	Note
a	Semimajor axis		au	Element 1
e	Orbital eccentricity		—	Element 2
I	Orbital inclination		deg	Element 3
Ω	Orbit LAN ^a		rad	Element 4
ω	Orbit AP ^b		rad	Element 5
ν	True anomaly		rad	Element 6
ϖ	Orbit LP ^c		rad	see text
N	Total No. of bodies ^d		—	
$\odot, \oplus, \mathbb{C}$	Sun, Earth, Moon/Lunar		—	or subscript $_{S,E,L}$
M_{\odot}	Central mass		1.0 or kg	
m_i	Mass of body i		M_{\odot} or kg	
n_i	Mean motion		rad d ⁻¹	
ϵ	Obliquity angle		deg	
ϵ_0	Obliquity Earth t_0	23.4392911	deg	Fränz and Harper (2002)
ϕ	Precession angle ^e			
Ψ_0	Luni-solar prec. rate t_0 ^f	50.3848	" y ⁻¹	Capitaine et al. (2003)
Ψ_A	Accumulated angle		"	$\dot{\Psi}_A = \Psi$
p_A	General prec. in long. ^g		"	$p_A = -\phi$
$\bar{\omega}$	Orbit LPX ^h			$\bar{\omega} = \varpi + \phi $ ^e
\bar{p}	Climatic precession			$\bar{p} = e \sin \bar{\omega}$
\mathbf{s}	Spin vector			
\mathbf{n}	Orbit normal			
H	Dynamical ellipticity	~0.00328	—	
k^2	(Gauss grav. const.) ²	0.01720209895 ²	see ⁱ	
au	Astronomical unit	$1.495978707 \times 10^{11}$	m	
GM_{\odot}	Sun GP ^j	$1.32712440041 \times 10^{20}$	m ³ s ⁻²	
$M_{\odot}/(m_{\oplus} + m_{\mathbb{C}})$	Mass ratio	328900.5596	—	
$m_{\oplus}/m_{\mathbb{C}}$	Mass ratio	81.300568	—	
Ω_E	Earth's angular speed	7.292115×10^{-5}	rad s ⁻¹	at t_0

^a LAN = Longitude of Ascending Node. ^b AP = Argument of Perihelion. ^c LP = Longitude of Perihelion. ^d Including the central mass. ^e Axial precession is retrograde (Section 3.1, Fig. 14), hence $\dot{\phi}_0$ is taken negative here (time derivatives are denoted by "dot", $\dot{\phi} = d\phi/dt$). ^f Conventionally, Ψ is taken positive (Section 3.1). ^g General precession in longitude. ^h LPX = LP from the moving equinox. $\bar{\omega}$ ("omega bar") is not be confused with ϖ ("varpi"). Various symbols are used for $\bar{\omega}$ in the literature. ⁱ General unit of k : au^{3/2} d⁻¹ M₀^{-1/2}, dimensionless in astronomical units, also rad d⁻¹ when e.g., equated with n_i . ^j GP = Gravitational Parameter.

scales $\gtrsim 10$ kyr. Based on work from the late 1800s, a new \mathcal{AS} was calculated by Brouwer and van Woerkom (1950) and subsequently applied to test the astronomical theory of climate change (e.g., van Woerkom, 1953; Broecker, 1966). Importantly, the \mathcal{AS} s up to that point were based on so-called low-order perturbation theory, sometimes dubbed secular analytic theory, or Laplace-Lagrange solution (for details and history, see Murray and Dermott, 1999; Ito and Tanikawa, 2007), which only allows for quasi-periodic, i.e., non-chaotic, solutions. A simple example of a quasi-periodic function is the sum of two periodic functions (single frequency each) with an irrational frequency ratio.

From a practical perspective, the next significant step in \mathcal{AS} development followed in the 1970s and provided Earth's orbital parameters over the past few million years at improved accuracy (Bretagnon, 1974; Berger, 1976, 1977). The \mathcal{AS} s were still based on secular

perturbation theory but included higher-order terms in series expansions with respect to eccentricity, inclination, and planetary masses (Bretagnon, 1974; Duriez, 1977; Laskar, 1985). Taking advantage of the accelerating computer power in the 1980s, Sussman and Wisdom (1988) studied the outer planets using full numerical integrations over 845 Myr on the Digital Orrery and showed that the motion of Pluto is chaotic. (The Digital Orrery was a special-purpose computer built specifically for studying planetary motion (Applegate et al., 1985), named after *orrery*, a mechanical model of the solar system that illustrates the relative positions and motions of the planets and moons.) Higher-order, averaged equations of the secular evolution of the inner and outer planets also showed chaos, with a “Lyapunov time” for the inner solar system of only ~ 5 Myr (Laskar, 1989).¹ The Lyapunov time is a metric to characterize chaos in dynamical systems and represents the time scale of exponential divergence (e-folding time) of nearby trajectories (see, e.g., Murray and Dermott, 1999).

The first fully numerical and “direct” long-term integration (the past 3 Myr) of the eight planets and Pluto *directly* based on the equations of motion (not analytical) was carried out by Quinn et al. (1991) using a multistep method. Quinn et al. (1991) showed that the model and secular theory predictions of, e.g., Earth’s orbital eccentricity and obliquity by Berger (1978), were inaccurate beyond about 1-1.5 Myr in the past, although subsequent updates by Berger and Loutre (1992) showed better agreement with Quinn et al. (1991). Notably, the \mathcal{AS} s based on earlier physics models and low/intermediate-order analytic secular perturbation theory were (a) by design unable to reveal the chaotic behavior of the the solar system and (b) were only accurate over the past few Myr. These results suggested that either fully numerical approaches or very high-order secular solutions were required for accurate applications in the Earth sciences. Laskar (1990) provided a long-term orbital solution that was obtained using an extended, averaged secular system. Regarding long-term solar system integrations, we note that Ito and Tanikawa (2002) performed full numerical, long-term integrations of up to 5 Gyr of the eight planets and Pluto. However, the study’s focus was long-term stability, rather than accuracy for geological applications and omitted several second-order effects (i.e., general relativity, a separate Moon, and asteroids). In 2003, Varadi and co-workers published the results of a direct, fully numerical integration of the eight planets over the past 100 Myr using a Störmer multistep scheme, which revealed large differences to the results of Laskar (1990) already around -24 Myr (Varadi et al., 2003) (past time in \mathcal{AS} s is negative here, see footnote 1). The early 2000s effectively marked the end of \mathcal{AS} based on secular perturbation theory for any serious geological application. Subsequent \mathcal{AS} employed in, for instance, astrochronology and cyclostratigraphy are based on full numerical integrations (Laskar et al., 2004; Laskar et al., 2011; Zeebe, 2017; Zeebe and Lourens, 2019, 2022a,b; Zeebe and Lantink, 2024a,b). The most recent numerical solutions are described in more detail in Section 2.5.

Over the past few decades, the improvement in accuracy of \mathcal{AS} s has permitted the development of the astronomical time scale (ATS, see Table 2), which has transformed the dating of geologic archives. Simply put, the ATS represents an accurate astronomical calendar used in

¹“Myr” (million years) is used here for duration, length of time intervals, and numerical time in \mathcal{AS} s (negative in the past), whereas “Ma” (mega annum) is used for geohistorical dates; correspondingly for kyr, ka, Gyr and Ga (Aubry et al., 2009).

Table 2: Frequently used acronyms

Acronym	Meaning
\mathcal{AS}	Astronomical Solution
AM	Amplitude Modulation
ATS	Astronomical Time Scale
EC	Eccentricity Cycle
ETP	Eccentricity, Tilt, Precession
FM	Frequency Modulation
FFT	Fast Fourier Transform
LEC	Long Eccentricity Cycle
OS	Orbital Solution
PT	Precession-Tilt
SEC	Short Eccentricity Cycle
VLEC	Very Long Eccentricity Cycle
VLN	Very Long eccentricity Node

the Earth sciences based on the motion of solar system bodies to study and explain Earth’s geologic history (for further reading, see, e.g., [Montenari, 2018](#)). In addition to accurate relative (floating) age models and chronologies (see also Section 3.5), astrochronology provides highly accurate geological dates with small error margins. For example, recent efforts have dated the Paleocene-Eocene Thermal Maximum (PETM) onset at 56.01 ± 0.05 Ma and the Cretaceous-Tertiary Boundary at 65.96 to 65.52 Ma ([Zeebe and Lourens, 2019, 2022b](#)). “Tertiary” is used informally here, not as a formal division ([ICS, 2005](#)). Astrochronology has made formidable progress in geological dating through deep-sea drilling and age-model tuning to \mathcal{AS} s, which led to the calibration of critical intervals of the geologic time scale, particularly in the early and mid-Cenozoic (e.g., [Hinnov, 2000](#); [Zachos et al., 2001](#); [Lourens et al., 2005](#); [Westerhold et al., 2008](#); [Hilgen et al., 2010](#); [Hilgen et al., 2015](#); [Liebrand et al., 2016](#); [Meyers and Malinverno, 2018](#); [Lauretano et al., 2018](#); [Li et al., 2018](#); [Hinnov, 2018](#); [Zeebe and Lourens, 2019](#); [Westerhold et al., 2020](#); [Zeebe and Lourens, 2022a,b](#)).

Importantly, an increasing number of studies at the current frontier of cyclostratigraphic research are pushing the boundaries into deep time, thereby providing unique insight into astronomical forcing of paleoclimate and solar-system evolution over hundreds of millions to billions of years (e.g., [Zhang et al., 2015](#); [Ma et al., 2017](#); [Meyers and Malinverno, 2018](#); [Kent et al., 2018](#); [Lantink et al., 2019](#); [Olsen et al., 2019](#); [Sørensen et al., 2020](#); [Lantink et al., 2022, 2023, 2024](#); [Zeebe and Lantink, 2024a,b](#); [Malinverno and Meyers, 2024](#); [Wu et al., 2024](#)). A critical ongoing task is to use the geological record to confirm and map the solar system’s chaotic behavior, reconstruct the Earth-Moon history, and develop a “Geological Orrery”, in analogy to the mechanical and Digital Orrery (see above and [Olsen et al., 2019](#)). For more information on astronomical forcing and astronomical solutions in deep time, see Section 3.5.

Today, \mathcal{A} S and the ATS represent the backbone of astrochronology and cyclostratigraphy, and are widely used in the Earth sciences, including areas of geology, geophysics, paleoclimatology, paleontology, and more. The applications are broad, ranging from high-fidelity dating (establishing highly accurate geological ages and chronologies) and reconstructing forcing/insolation patterns and their effects on paleoclimate — to the evolution of the Earth-Moon system and nonlinear dynamics (to name just a few, for recent summaries, see [Montenari, 2018](#); [Hinnov, 2018](#); [Cvijanovic et al., 2020](#); [Lourens, 2021](#); [De Vleeschouwer et al., 2024](#); [Wu et al., 2024](#)).

1.1. The Main Milanković Cycles

The focus of this review is on astronomical solutions and forcing, rather than on the forcing’s effects on Earth’s climate through insolation changes. Nevertheless, the main Milanković cycles are very briefly summarized here (for details and reviews, see, e.g., [Milanković, 1941](#); [Hays et al., 1976](#); [Broecker, 1985](#); [Berger and Loutre, 1994](#); [Muller and MacDonald, 2002](#); [Hinnov, 2018](#); [Lourens, 2021](#)). As mentioned above, the main Milanković cycles usually refer to precession, obliquity, and eccentricity (for illustration and main periods, see Fig. 1). To be precise, we refer here to climatic precession (see Section 3.1). Climatic precession and obliquity affect the geographical distribution of insolation over time, whereas eccentricity affects the total insolation Earth receives (precession and obliquity do not). For instance, climatic precession shifts the positions of the equinoxes relative to Earth’s eccentric orbit (see Figs. 1 and 14). Hence, if at a given time northern hemisphere summer occurs at perihelion, it will occur at aphelion about 10 kyr later (perihelion and aphelion refer to the closest and farthest distance from the Sun along Earth’s orbit, see Fig. 2). As a result, the insolation at a given calendar day and latitude on Earth varies with climatic precession over time (one critical element in the pacemaking of the ice ages, e.g., [Hays et al., 1976](#)). The effects of climatic precession are anti-phased between the hemispheres.

Obliquity changes the solar incidence angle of insolation at a given latitude on Earth (see Figs. 1 and 14). Obliquity thus affects the seasonal contrast of insolation (in-phase between the hemispheres and increasingly pronounced toward higher latitudes). For instance, at an obliquity angle $\epsilon = 0^\circ$, the tilt-induced seasons would disappear, whereas at $\epsilon = 90^\circ$, the tilt-induced seasons would be extreme (as is the case on Uranus with an obliquity of $\sim 98^\circ$). Earth’s recent obliquity varies between minima and maxima of about 22.0° and 24.5° over a 41-kyr main period (Fig. 1), which causes substantial changes in Earth’s climate — often enhanced when continental ice sheets are present (for summaries, see, e.g., [Lourens, 2021](#); [De Vleeschouwer et al., 2024](#)). Local insolation changes due to obliquity (and climatic precession) may be sizable. For example, at 65°N (Jun 21) insolation varies up to $\sim 120 \text{ W m}^{-2}$ over the past 1 Myr.

Earth’s orbital eccentricity (e_\oplus) impacts insolation in multiple ways. For example, on precessional time scales, e_\oplus modulates the amplitude of precession, which, in turn, affects insolation (Fig. 1). On annual time scales, e_\oplus influences the total insolation Earth receives along its orbit, as the distance (r) to the Sun varies (see Fig. 1 and 2, for $e_\oplus \neq 0$). At perihelion and aphelion r is equal to $a(1 - e_\oplus)$ and $a(1 + e_\oplus)$, respectively, where a is the semimajor axis (e.g., [Danby, 1988](#)). Given that the insolation with respect to Earth’s cross

section at distance r is proportional to r^{-2} , the insolation ratio at perihelion vs. aphelion is:

$$(1 + e_{\oplus})^2 / (1 - e_{\oplus})^2, \quad (1)$$

which yields $\sim 7\%$ and 27% at present $e_{\oplus} = 0.0167$ and $\max\{e_{\oplus}\} \simeq 0.06$, respectively (see Fig. 1). As a result, eccentricity also induces “seasons”, which are, however, hemispherically symmetric and presently smaller than the tilt-induced seasons. The *total mean annual insolation* (or energy W) Earth receives is proportional to (e.g., [Berger and Loutre, 1994](#)):

$$W \propto (1 - e_{\oplus}^2)^{-\frac{1}{2}}. \quad (2)$$

The absolute effect of the factor $(1 - e_{\oplus}^2)^{-\frac{1}{2}}$ at present is small ($\sim 0.014\%$), compared to a circular orbit with $e_{\oplus} = 0$. However, for long-term variations, the ratio of W at different e_{\oplus} ’s matters. For example, between the present $e_{\oplus} = 0.0167$ and $e_{\oplus} = 0.06$, W increases by $\sim 0.17\%$, which is *not* negligible because it raises the total, global energy received. At a solar constant of 1370 W m^{-2} , 0.17% amounts to 2.3 W m^{-2} (0.6 W m^{-2} when distributed over Earth’s surface, i.e., reduced by factor 4). For comparison, a doubling of CO_2 in Earth’s atmosphere is equivalent to $\sim 3.7 \text{ W m}^{-2}$ of radiative forcing. Thus, orbital eccentricity forcing (in W m^{-2}) may appear small compared to local changes from climatic precession and obliquity (see above). However, the difference is that eccentricity forcing is global. Finally, and regardless of whether precession, obliquity, or eccentricity forcing is involved, caution is advised when attempting to predict the impact of astronomical forcing on Earth’s climate, because the climate system response is highly non-linear.

Regarding the stratigraphic recording of the climate system response (say, in sedimentary sequences), it is noteworthy that the response of the sedimentary system to climate perturbations is also inherently non-linear. Thus, the translation of astronomical cycles to sedimentary cycles is modified by two non-linear transfer functions.

1.2. Types of Astronomical Solutions

Two types of astronomical solutions are discussed in the following: orbital solutions (OSs) and precession-tilt (PT) solutions. OSs describe the orbital dynamics of the solar system, usually considering the solar system bodies as mass points (as is the case here). OSs provide values for the orbital elements of solar system bodies over time, including orbital eccentricity and inclination (see Fig. 2). PT solutions describe the rotational dynamics of individual solar system bodies (here of the Earth), considering the physical dimensions and shape of the body. PT solutions provide values for precession and obliquity over time, e.g., based on spin axis dynamics (see Fig. 14). OS dynamics have important effects on (and are a prerequisite for) PT solutions, while the effect of rotational dynamics on OSs is generally minor (e.g., Earth-Moon dynamics, see [Zeebe and Lantink, 2024b](#)). For example, amplitude variations in Earth’s orbital inclination (due to OS dynamics) are reflected in obliquity — most evidently during intervals of reduced amplitude variation (see [Zeebe, 2022](#)). Similarly, amplitude variations in eccentricity (due to OS dynamics) are reflected in climatic precession.

1.3. Organization of Content

The remainder of this review is organized into three sections focusing on orbital solutions, precession-tilt solutions, and practical considerations (Sections 2, 3, and 4). Section 2 introduces several basic concepts for describing and analyzing orbital solutions, including orbital elements and the fundamental frequencies of the solar system. Solar system chaos is key and indispensable to understanding a variety of topics, including the limitations imposed on orbital solutions by chaotic dynamics. Chaos is therefore discussed in some detail under orbital solutions (Section 2.3). Chaos also causes critical changes in the amplitude modulation (AM) of orbital forcing signals, which, if expressed in cyclostratigraphic sequences, can be used to reconstruct the solar system’s chaotic history. Section 2.3 on solar system chaos thus precedes Section 2.4 on amplitude and frequency modulation. Furthermore, AM originates from combination terms related to the fundamental frequencies but can also be studied using eccentricity and obliquity analysis. Thus, AM is examined in some depth in two sections (2.1.4 and 2.4.1). Up-to-date orbital solutions, their valid time span (another consequence of solar system chaos), and the confusion surrounding the subject are described in Section 2.5. Importantly, the probability that a particular OS represents the actual, unique history of the solar system is near zero significantly beyond the OS’s valid time span (the details and implications are explained in Sections 2.5 and 4). Section 3 dives into the details of precession-tilt solutions, explaining the various quantities associated with Earth’s axial precession and aiming at clarifying the terminology and notation used in the literature. Up-to-date precession-tilt solutions are described in Section 3.4, as well as recently employed tools that produce inaccurate results. Another critical application of astronomical solutions beyond the direct use for astronomical tuning (e.g., absolute Cenozoic ages and chronologies) is astronomical forcing and astrochronology in deep time (see Section 3.5). Section 4 provides several recommendations for the user seeking guidance and lists selected resources for practical consideration. We close with a brief summary and outlook (Section 5).

2. Orbital Solutions

2.1. Fundamentals

2.1.1. Orbital Elements

For the reader unfamiliar with orbital parameters commonly used in astronomy, we first introduce the Keplerian elements and the notation used throughout this paper (see Fig. 2 and Table 1). Keplerian orbits include circular ($e = 0$), elliptic ($0 < e < 1$, $a > 0$), parabolic ($e = 1$), and hyperbolic ($e > 1$, $a < 0$) orbits. To describe the orbit, six independent elements are used, five of which (for instance, a , e , I , Ω , and ω) define the shape and orientation of the orbit in space (for illustration, see Fig. 2). The final element (such as the true anomaly ν) identifies the body’s position in the orbit and hence represents the instantaneous (rapidly changing) orbital element. Notably, the Keplerian elements are used to describe orbits in general, not only exact solutions to Kepler’s two-body problem, which can be solved analytically. In the two-body problem ($N = 2$), ν varies over time, while the five elements defining orbit shape and orientation are constant, which is not the case in general ($N > 2$). For example, the motion of solar system bodies such as the planets include the full planet-planet interactions and hence do not evolve on simple Kepler ellipses. Nevertheless, at a given instant in time,

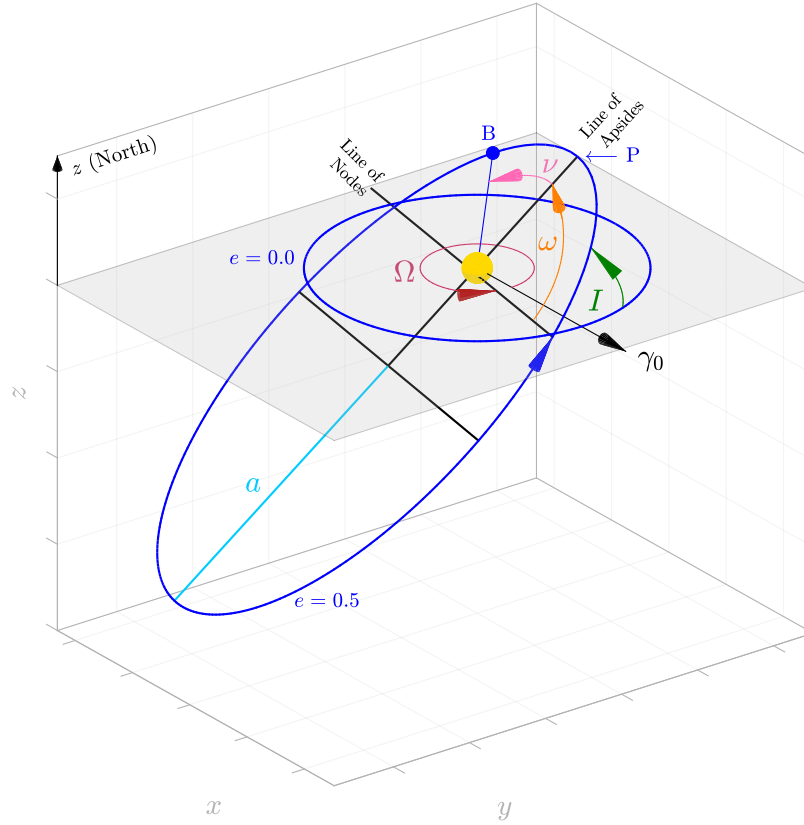


Figure 2: Illustration of elements characterizing a Keplerian orbit. a = semimajor axis, e = eccentricity, I = inclination. I is the angle measured from the fixed reference plane (gray) to the instantaneous orbit plane. Two orbits (blue, different a 's) are shown; the circular orbit ($e = 0$, $I = 0$) lies in the reference plane; the elliptic orbit ($e = 0.5$) is inclined relative to the reference plane. Ω = longitude of the ascending node is measured in the reference plane from the reference point γ_0 to the line of nodes where the orbiting body (B) ascends, i.e., passes from south to north ($z < 0$ to $z > 0$, see blue arrow) through the reference plane. Hence Ω (if defined) is measured in a plane different from B's orbital plane. In the solar system, γ_0 may refer to the vernal point at a fixed date. ω = argument of perihelion is measured from the ascending node to the perihelion (P). The line of apsides passes through the perihelion (P) and aphelion of the orbit (closest and farthest distance from the central body). ν = true anomaly is measured from the perihelion to the orbiting body (B).

the orbit can be defined by Keplerian (also called osculating) elements, which refer to the orbit the body would have without perturbations (in mathematics osculate means to touch so as to have a common tangent). In the general case, the orbit's shape and orientation change over time. The six orbital elements can be converted into the body's Cartesian position and velocity vectors \mathbf{x} and \mathbf{v} (and vice versa) via a coordinate transformation (six degrees of freedom). Thus, the output of orbital solutions may be provided in orbital elements or Cartesian vectors, or both.

Note that for $I = 0$, the line of nodes and hence Ω and ω are undefined. Nevertheless, as long as $e \neq 0$, the longitude of perihelion, ϖ , may always be defined (see Section 2.3 in [Bate et al., 1971](#)). ϖ is measured from the reference point to the perihelion eastward (to the ascending node, if it exists, and then in the orbital plane to the perihelion). If both Ω and ω are defined, then

$$\varpi = \Omega + \omega . \quad (3)$$

In general, ϖ is therefore a “dogleg” angle, as Ω and ω lie in different planes. However, this

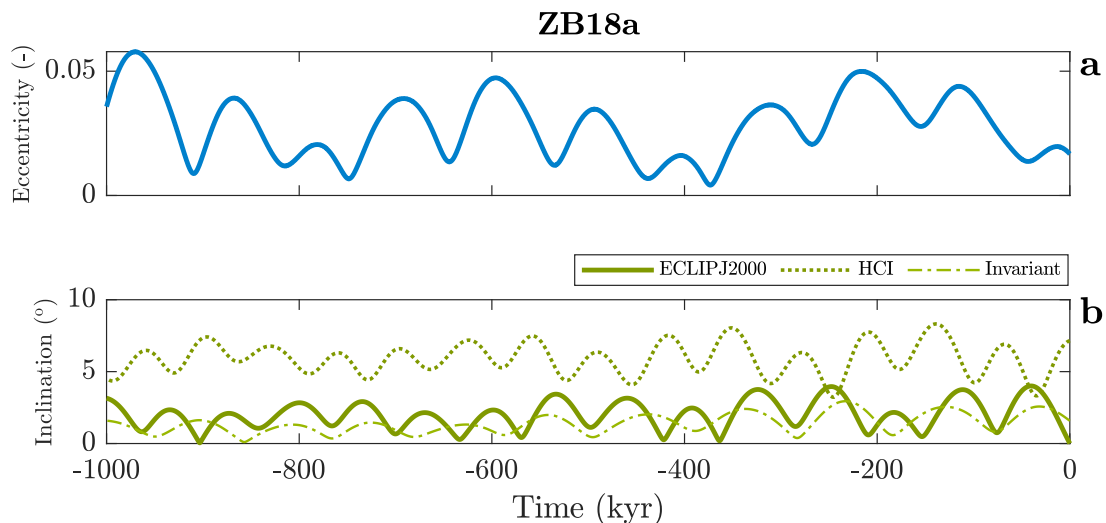


Figure 3: Earth’s orbital eccentricity and inclination from *AS ZB18a* (Zeebe and Lourens, 2019) over the past 1 Myr. For geometrical illustrations of the physical meaning of orbital eccentricity and inclination, see Figs. 2, 4, and 14. (a) Earth’s orbital eccentricity (which is independent of the reference frame). (b) Earth’s orbital inclination in different reference frames. Solid line: Ecliptic frame (ECLIPJ2000), dashed line: Heliocentric Inertial (HCI) frame (for details, see Fränz and Harper, 2002; Zeebe, 2017), dot-dashed line: invariant frame (see text).

does not impede its use and utility as an orbital element. Importantly, ϖ is well defined for all inclinations.

2.1.2. Eccentricity and Inclination

Earth’s orbital eccentricity is among the most frequently used orbital parameters in Earth-science applications (see Fig. 3 for an example over the past 1 Myr). Cyclostratigraphic sequences, for instance, often show strong cyclicity at eccentricity frequencies (main periods of ~ 100 kyr and 405 kyr in the recent past). Eccentricity affects the total insolation Earth receives over one year (e.g., Berger and Loutre, 1994), which in turn affects Earth’s climate (Section 1.1). Moreover, if clear axial precession signals are present in the geologic sequence, the observed precession amplitude is modulated by eccentricity (in a very simple manner, i.e., eccentricity is the envelope of climatic precession, see Fig. 1). Eccentricity is related to the shape of the orbit (not the orientation in space, see Fig. 2) and is hence independent of the reference frame used to describe the orbit. In contrast, orbital inclination depends on the reference frame, as the choice of the reference plane is arbitrary (Fig. 2). Thus, the representation of inclination may differ fundamentally between different reference frames (for a frequently used frame such as the ecliptic, see Fig. 3). However, other frames such as the invariant frame (based on the invariable plane, perpendicular to the solar system’s total angular momentum vector that passes through its barycentre) or the Heliocentric Inertial (HCI) frame (based on the orientation of the solar equator at a fixed point in time) are equally valid and are useful for e.g., accounting for effects of the solar quadrupole moment on the dynamics (for details, see Fränz and Harper, 2002; Souami and Souchay, 2012; Zeebe, 2017). Note that accurate transformations between frames generally require detailed information about the coordinate systems and, depending on the case, parameters such as initial conditions, masses, constants used, etc. (see below and Souami and Souchay (2012)).

Because of the distinct physical nature of inclination and eccentricity (see Fig. 2), orbital forcing effects (Section 1.1) due to inclination and eccentricity are principally different (for

further discussion, see, e.g., [Muller and MacDonald, 2002](#); [Zeebe, 2022](#); [Zeebe and Lantink, 2024b](#)). Orbital inclination represents one of the controls on the obliquity of Earth’s spin axis but the relationship is more complex than between eccentricity and climatic precession ($\bar{p} = e \sin \bar{\omega}$). For example, the obliquity amplitude (variation around the mean) depends on the main inclination amplitude and frequency but also on the luni-solar precession rate (see Section 3 and e.g., [Ward, 1974, 1982](#); [Zeebe, 2022](#); [Zeebe and Lantink, 2024b](#)). In addition to their role as individual orbital parameters, orbital inclination and eccentricity are key to understanding the fundamental (secular) frequencies of the solar system (Section 2.1.3).

Different eccentricity cycles (ECs) may be expressed and hence be observable in cyclostratigraphic sequences, i.e., the short EC (SEC), long EC (LEC) and very long EC (VLEC). The forcing periods of the two main SEC pairs in the recent past are about 95/99 kyr and 124/131 kyr, while the dominant LEC forcing period in the recent past is ~ 405 kyr (see Section 2.1.4). Until recently, the widely accepted and long-held view was that the LEC was practically stable in the past and has been suggested for use as a “metronome” (see Section 2.2) to reconstruct accurate ages and chronologies, including deep-time geological applications ([Laskar et al., 2004](#); [Kent et al., 2018](#); [Spalding et al., 2018](#); [Meyers and Malinverno, 2018](#); [Montenari, 2018](#); [Lantink et al., 2019](#); [De Vleeschouwer et al., 2024](#)). However, it has recently been demonstrated that the LEC can become unstable over long time scales ([Zeebe and Lantink, 2024a](#)). The VLEC refers to the long-term amplitude modulation of eccentricity (recent period of ~ 2.4 Myr) and is related to the secular frequency term ($g_4 - g_3$) (see Section 2.1.3). The VLEC is unstable and its expression in cyclostratigraphic sequences may be used to reconstruct the solar system’s chaotic history beyond ~ 50 Ma ([Ma et al., 2017](#); [Westerhold et al., 2017](#); [Olsen et al., 2019](#); [Zeebe and Lourens, 2019](#)). For more information on the unstable VLEC and the resonance involving ($g_4 - g_3$), see Section 2.4.1.

2.1.3. Secular Frequencies: g and s Modes

As mentioned above, in planetary systems with $N > 2$, the shape and orientation of the orbits change over time due to mutual interactions. For example, the eccentricity and inclination of each orbit generally varies and the line of apsides and the line of nodes are not fixed in space as in the two-body problem (see Fig. 2). The lines generally precess, aka apsidal and nodal precession, respectively. Given that the Newtonian interaction between the orbiting bodies depends on mass and distance, one would expect that the frequencies at which the orbital elements change over time would depend on, for instance, m_i and a_i . Indeed, an analytical calculation to determine, for example, the frequencies for $N = 3$ (including one dominant mass) using low-order secular perturbation theory for small e_i and I_i shows a frequency dependence on only m_i and a_i , and n_i , where $n_i = (k^2 M_\odot / a_i^3)^{1/2}$ ([Murray and Dermott, 1999](#)). The frequency spectrum of each body is composed of different contributions from the fundamental (secular, slowly changing) frequencies of the full system (aka fundamental proper modes, or eigenmodes). The secular frequencies may be thought of as the spectral building blocks of the system as given (dominated by the m ’s and a ’s of the major bodies, e.g., the planets in the solar system). Importantly, however, there is generally no simple one-to-one relationship between, say, an eigenmode and a single planet, particularly for the inner planets (note that there is no apsidal and nodal precession for a single body). The system’s motion is a superposition of all eigenmodes, although some modes

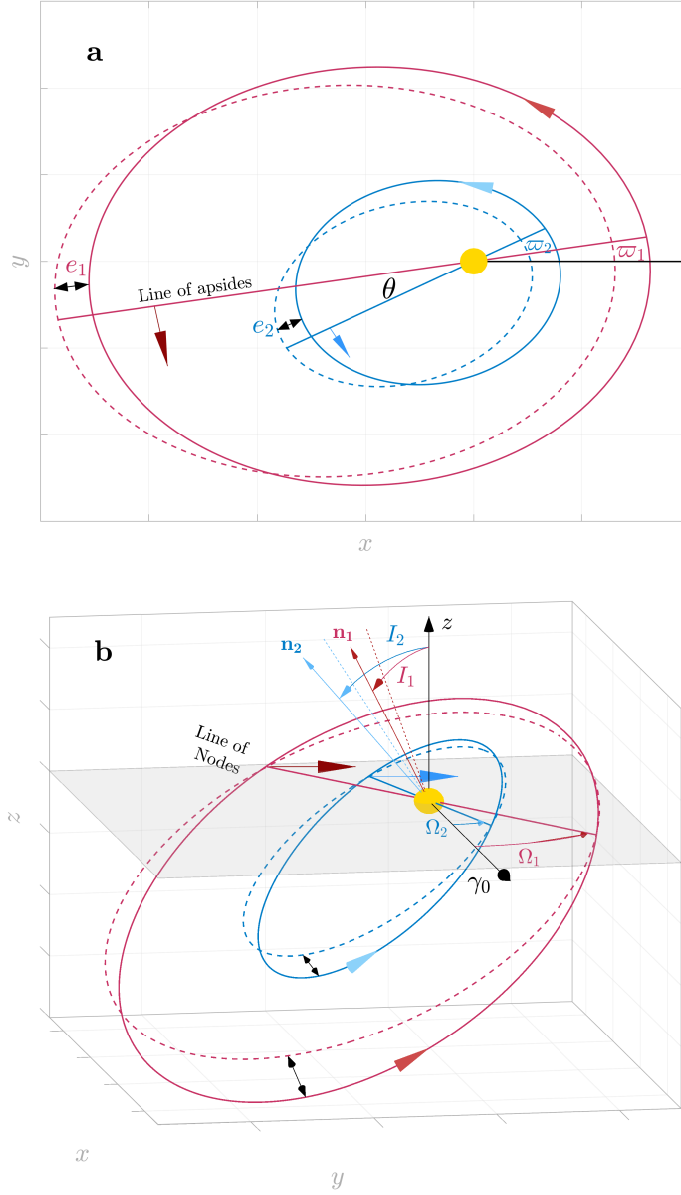


Figure 4: Schematic illustration of g and s modes for $N = 3$ (for symbols and notation, see Table 1 and Fig. 2). Note that there is generally no simple one-to-one relationship between eigenmode and a single planet (see text). (a) g modes (inclinations zero, viewed from ecliptic north; $\theta = \varpi_2 - \varpi_1$). The apsidal precession is prograde (counterclockwise) in the same direction as the orbital motion (light blue and red arrows). (b) s modes. The nodal precession is retrograde (clockwise) in the opposite direction as the orbital motion (light blue and red arrows). The orbit normals \mathbf{n}_i hence describe a precessional/nutational motion (here about the z -axis).

represent the single dominant term for some (mostly outer) planets. The breakdown into eigenmodes is similar to the problem of N coupled oscillators in physics, where the overall motion/spectrum may be complex but can be decomposed into the superposition of N characteristic, fundamental frequencies. In celestial mechanics, the lowest-order solution (in e and I) to the N -body problem (with a dominant central mass and small e_i and I_i) is called Laplace-Lagrange solution (e.g., Murray and Dermott, 1999).

The secular frequencies of the solar system naturally split into g and s modes, which are loosely related to the apsidal and nodal precession of the orbits, respectively (see Fig. 4).

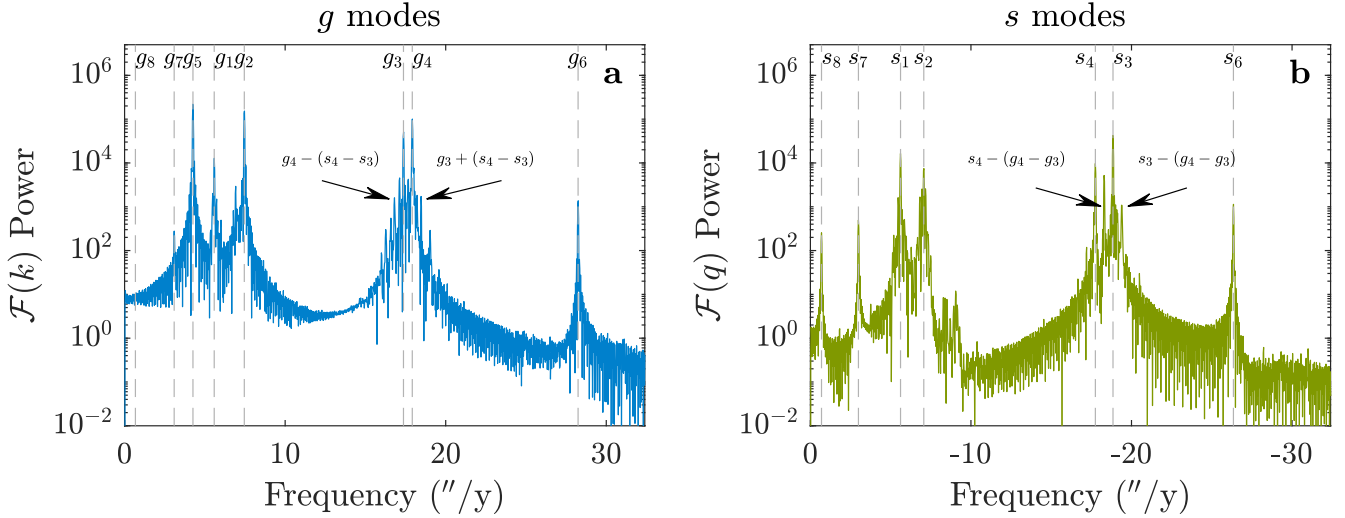


Figure 5: Time series analysis of (a) k and (b) q for Earth (see Eqs. (4) and (5)) to extract solar system secular (or fundamental) frequencies from numerical integrations (solution ZB18a). Time interval: $[-20\ 0]$ Myr. \mathcal{F} = Fast-Fourier Transform (FFT). Vertical dashed lines indicate frequencies (see Table 3). Note that s frequencies (b) are negative (retrograde nodal precession). Also note significant side peaks due to $(g_4 - g_3)$ around the main peaks s_3 and s_4 . Side peaks around g_3 and g_4 in (a) are also present due to $(s_4 - s_3)$, illustrating the interaction of g and s modes. For a ratio $(s_4 - s_3) : (g_4 - g_3) = 2:1$, $s_4 - (g_4 - g_3) = s_3 + (g_4 - g_3)$.

The g and s frequencies are constant in quasi-periodic systems but vary over time in chaotic systems and as such are critical for understanding the long-term behavior of the solar system. The g 's and s 's may be obtained by spectral analysis of the classic variables for each planet (see Fig. 5 and Table 3):

$$h = e \sin(\varpi) \quad ; \quad k = e \cos(\varpi) \quad (4)$$

$$p = \sin(I/2) \sin \Omega \quad ; \quad q = \sin(I/2) \cos \Omega \quad (5)$$

for e , I , ϖ , and Ω , see Figs. 2, 4, and Table 1. In the Laplace-Lagrange solution, the h, k, p , and q can be written as simple trigonometric sums with constant g 's and s 's (e.g., Murray and Dermott, 1999).

Keeping in mind the generally complex relation between individual planets and eigenmodes, the g and s modes may be schematically illustrated (see Fig. 4 for $N = 3$). The g modes involve variations in e and ϖ , where e usually varies between some extreme values (black double arrows, Fig. 4a) and ϖ characterizes the apsidal precession; ϖ may librate (oscillate) or circulate for solar system orbits. In the linear system and for a simple eigenmode-planet relationship, the time average $\langle \varpi_i \rangle$ may be written as $\langle \varpi_i \rangle \simeq g_i t$, or $\langle \dot{\varpi}_i \rangle \simeq g_i$ (where “dot” denotes the time derivative). The planetary g_i 's ($i = 1, \dots, 8$) are positive (see Table 3), hence for circulating ϖ , the time-averaged apsidal precession is prograde (i.e., in the same direction as the orbital motion, see large arrows in Fig. 4a). The frequency g_9 (dominated by Pluto) is negative (Table 3). Importantly, however, the values and signs of the solar system's fundamental frequencies are not deduced from the motion of individual planets, but from the eigenmode analysis of the full system.

The lines of apsides of two orbits coincide, i.e., their perihelia are aligned, for $\theta = \varpi_2 - \varpi_1 = 2\pi \cdot n$, where n is an integer (see Fig. 4a), or in the simple, linear system at $(g_2 - g_1)t = 2\pi \cdot n$, i.e., at a frequency $(g_2 - g_1)$. Thus, one might expect that a major component in a

Table 3: Solar system secular (or fundamental) frequencies ($\text{arcsec y}^{-1} = '' \text{y}^{-1}$)^a and periods (y) from ZB18a. Interval: $[-20 \text{ } 0]$ Myr.

#	g $b('' \text{y}^{-1})$	T_g (y)	s $('' \text{y}^{-1})$	T_s (y)
1	5.5821	232,170	−5.6144	230,837
2	7.4559	173,821	−7.0628	183,498
3	17.3695	74,613	−18.8476	68,762
4	17.9184	72,328	−17.7492	73,017
5	4.2575	304,404	0.0000	—
6	28.2452	45,884	−26.3478	49,188
7	3.0878	419,719	−2.9926	433,072
8	0.6736	1,923,992	−0.6921	1,872,457
9	−0.3494	3,709,721	−0.3511	3,691,356

^a 1 arcsec = 1/3600 of a degree.

^b Frequency conversion from kyr^{-1} to arcsec y^{-1} is $(\times 3600 \cdot 360/1000 = 1296)$.

planet’s orbital eccentricity spectrum occurs at the difference between two secular frequencies (relative motion). Indeed, the highest power in, e.g., Earth’s recent orbital eccentricity spectrum occurs at about $3.2 '' \text{y}^{-1}$ (arcsec y^{-1} , see Table 4), or a period of ~ 405 kyr (see Fig. 6). It turns out that this frequency is associated with $(g_2 - g_5)$; the values given in Table 3 yield $(g_2 - g_5) = 7.4559 - 4.2575 = 3.1984 '' \text{y}^{-1}$, or 405 kyr. The $(g_2 - g_5)$ cycle is also called long eccentricity cycle (see Section 2.1.2) and represents the most stable g mode combination term in Earth’s eccentricity spectrum in the recent past (although for deep time, see Zeebe and Lantink, 2024a). The various combinations of $(g_i - g_j)$ and $(s_i - s_j)$ relevant for Earth’s orbital eccentricity and inclination are discussed in Sections 2.1.4 and 2.4.

The s modes involve variations in I and Ω , where I usually varies between some extreme values (black double arrows, Fig. 4b) and Ω characterizes the nodal precession; Ω may librate or circulate. In the simple, linear system, the time average $\langle \dot{\Omega}_i \rangle$ may be written as $\langle \dot{\Omega}_i \rangle \simeq s_i t$, or $\langle \dot{\Omega}_i \rangle \simeq s_i$. The planetary s_i ’s are negative (see Table 3), hence for circulating Ω , the time-averaged nodal precession is retrograde (i.e., in the opposite direction as the orbital motion, see large arrows in Fig. 4b). Given conservation of total angular momentum (\mathbf{L}), there exists an invariable plane perpendicular to \mathbf{L} , which is fixed in space. It follows that one of the s frequencies is zero (s_5 , see Table 3). Thus, the p and q solutions behave slightly different than the h and k solutions (see Eqs. (4) and (5)). The eccentricity of an orbit introduces a reference line and hence an asymmetry into the problem for the g modes (h, k), which is not the case for the s modes (p, q). For the latter, the mutual inclination between, say, two orbits matters, not the absolute inclination relative to an arbitrary reference plane (Murray and Dermott, 1999).

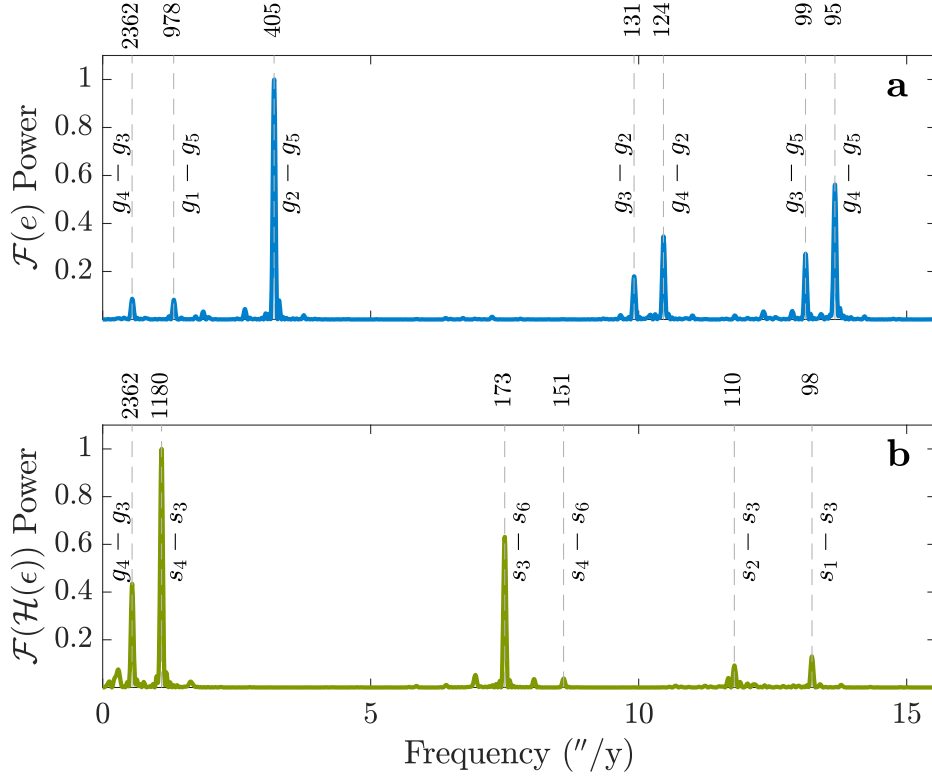


Figure 6: (a) FFT of Earth’s orbital eccentricity in the recent past ($\mathcal{F}(e)$). Interval: $[-20\ 0]$ Myr. (b) FFT of the Hilbert transform of Earth’s obliquity ($\mathcal{F}(\mathcal{H}(\epsilon))$). Spectral power is normalized to maximum power. Numbers above panels indicate periods in kyr.

2.1.4. Frequency Combination Terms: Eccentricity & Obliquity-Modulation

As discussed above, major components (terms) in relevant orbital parameter spectra usually occur at the difference between pairs² For instance, the main eccentricity terms in the recent past (405 kyr and ~ 100 kyr) are due to combination pairs of g frequencies (see Fig. 6a and Table 4). Importantly, the ~ 100 kyr band is actually composed of four individual frequencies, which, in geologic sequences, are identifiable separately however only in high-quality cyclostratigraphic records. The g -frequency combination terms that dominate orbital eccentricity (Fig. 3) are directly accessible through time series analysis of eccentricity (here FFT, $\mathcal{F}(e)$, Fig. 6). Note that in general, there is no analogous relationship between s -frequency combinations and inclination, again due to the dependence of inclination on the reference frame (see Section 2.1.2). A natural choice for extracting s -frequency combinations from inclination would be the invariant frame. However, orbital elements in the invariant frame are not universally provided by \mathcal{AS} s. Moreover, compared to eccentricity, there is also no equivalent expression of inclination in stratigraphic sequences that could be used for practical purposes.

A more useful approach for extracting s -frequency combinations from \mathcal{AS} s is analyzing the amplitude modulation of obliquity. This approach also makes practical sense because

²Multiple frequency combinations usually lead to minor terms, some of which may be observable in the geologic record (for a recently noticed ~ 200 -kyr cycle, see Hilgen et al., 2020). of secular frequencies (relative motion).

obliquity and its AM are often expressed in cyclostratigraphic records. To obtain the AM frequency terms of obliquity from \mathcal{AS} s, we first extract the envelope of obliquity by applying the Hilbert transform, $\mathcal{H}(\epsilon)$ (see also Fig. 12) and then apply FFT ($\mathcal{F}(\mathcal{H}(\epsilon))$), Fig. 6b and Table 4). The strongest obliquity AM terms in the recent past are (s_4-s_3) and (s_3-s_6) , which are discussed in more detail in Section 2.4. The next highest peak is due to g modes (not s modes), i.e., the combination (g_4-g_3) , which may be surprising if one expects only s terms to appear in the obliquity AM spectrum. However, as shown above, significant (g_4-g_3) side peaks are present around s_3 and s_4 (Fig. 5). In turn, the combination of the main- and side peaks then lead to significant power at the beat frequency (g_4-g_3) in the obliquity AM spectrum. The interaction of g and s modes, i.e., g frequencies appearing in q 's spectrum and s frequencies appearing in k 's spectrum (see Eqs. (4), (5), and Fig. 5) illustrate the non-linear behavior of solar-system dynamics (in the linear system, the g and s modes are decoupled and independent of each other). In fact, (s_4-s_3) and (g_4-g_3) are currently in a so-called 2:1 resonance state (periods of ~ 1.2 and ~ 2.4 Myr, Table 4), which is a major contributor to long-term solar-system chaos (see Sections 2.3 and 2.4).

Table 4: Frequency terms ($\text{arcsec y}^{-1} = ''\text{y}^{-1}$)^a and periods (kyr) based on g and s frequencies in ZB18a (interval: $[-20\ 0]$ Myr, see Table 3).

Term	Short-hand	Freq. ^b ($''\text{y}^{-1}$)	Period ^c (kyr)	Expressed in
(g_4-g_3)	g_{43}	0.5487	2362	Ecc.& Oblq.
(g_1-g_5)	g_{15}	1.3246	978	Eccentricity
(g_2-g_5)	g_{25}	3.1984	405	Eccentricity
(g_3-g_2)	g_{32}	9.9137	131	Eccentricity
(g_4-g_2)	g_{42}	10.4624	124	Eccentricity
(g_3-g_5)	g_{35}	13.1121	99	Eccentricity
(g_4-g_5)	g_{45}	13.6609	95	Eccentricity
(s_4-s_3)	s_{43}	1.0983	1180	Obliquity-AM
(s_3-s_6)	s_{36}	7.5003	173	Obliquity-AM
(s_4-s_6)	s_{46}	8.5986	151	Obliquity-AM
(s_2-s_3)	s_{23}	11.7847	110	Obliquity-AM
(s_1-s_3)	s_{13}	13.2331	98	Obliquity-AM

^a 1 arcsec = 1/3600 of a degree.

^b Frequency conversion from kyr^{-1} to arcsec y^{-1} is $(\times 3600 \cdot 360/1000 = 1296)$.

^c Uncertainties in (g_4-g_3) and (s_4-s_3) periods from spectral analysis may be estimated as ± 40 kyr and ± 10 kyr (Zeebe, 2022).

2.2. The so-called “Metronomes”

The term astrochronological *metronome* usually refers to a prominent and exceptionally stable frequency in Earth’s orbital parameters that may be widely used to construct accurate chronologies. Importantly, for the frequencies to be of use in practical applications requires both frequency and amplitude to be stable. The eccentricity term (g_2-g_5) (~ 405 kyr in the recent past) and the inclination term (s_3-s_6) (~ 173 in the recent past) have been labeled the

eccentricity- and inclination metronome, respectively (Laskar, 2020). However, Zeebe and Lantink (2024a) have recently shown that (g_2-g_5) can become unstable on long time scales, which compromises the 405-kyr cycle’s reliability beyond several hundred million years in the past. The term (s_3-s_6) is also unreliable, yet on even shorter time scales. For example, analysis of the obliquity modulation (illustrated in Fig. 6) of the solution ZB18a shows that the dominant term involving s_6 across the interval -66 to -56 Myr is (s_4-s_6) , and not (s_3-s_6) . Note that ZB18a has been geologically constrained to -66 Myr, which includes the interval in question from -66 to -56 Myr (see Zeebe and Lourens, 2022b, and Table 5). Shifts in the dominant terms are due to changes in s_3 and s_4 , which are known to be variable beyond ~ 50 Myr (see Fig. 6 of Zeebe and Lourens (2022b)). As a result, the dominant period involving s_6 may shift to ~ 151 kyr or even alternate over time between ~ 173 and ~ 151 kyr. In summary, the current evidence does not support the notion of generally stable and prominent metronomes for universal use in astrochronology and cyclostratigraphy. The term (s_3-s_6) is reliable only over the past 50 Myr or so, an interval over which the secular frequencies appear stable anyway. The term (g_2-g_5) is more stable but cannot be taken for granted beyond several 100 Myr due to solar system chaos.

2.3. Solar System Chaos

Large-scale dynamical chaos is an inherent characteristic of the solar system and fundamental to understanding the behavior of astronomical solutions and their limitations, which is described below. First, an example of a simple analog mechanical system is introduced to illustrate some basic aspects of chaos.

2.3.1. The Driven Pendulum: Poincaré Section

Fundamental contributions to the theory of dynamical systems (including the gravitational three-body problem and the solar system) were made by Henri Poincaré (1854-1912), whose work laid the foundations of chaos theory. Poincaré wrote: “It may happen that small differences in the initial conditions produce very great ones in the final phenomena. A small error in the former will produce an enormous error in the latter. Prediction becomes impossible ...” (Poincaré, 1914). The sensitivity to small differences in initial conditions or small perturbations is a key element of chaotic systems.

A simple mechanical system often used to illustrate such behavior is the driven rigid pendulum (e.g., Chirikov, 1979; Lichtenberg and Lieberman, 1983; Murray and Holman, 2001; Morbidelli, 2002). Consider first a simple rigid pendulum in a gravitational field with angle x to the vertical (equivalent to position) and momentum $p = m\dot{x}$, where m and l are its effective mass and length, respectively (for phase diagram, see Fig. 7a). For small to moderate energies (regime I), the pendulum librates around the equilibrium point $(x, p) = (0, 0)$, representing a single oscillator. The trajectories originating in regime I are considered to be in resonance (Murray and Holman, 2001). For large energies (regime II), the pendulum rotates clockwise ($p < 0$) or counterclockwise ($p > 0$). The structure that separates the two regimes is called the separatrix (Fig. 7a). For initial conditions starting on the separatrix, the pendulum approaches the unstable fixed point (Fig. 7a, red star) as $t \rightarrow \infty$ (upright position). The motion of the pendulum starting in the vicinity of initial conditions (x^0, p^0) in regime I or II far from the separatrix is quite simple. Starting at neighboring points in

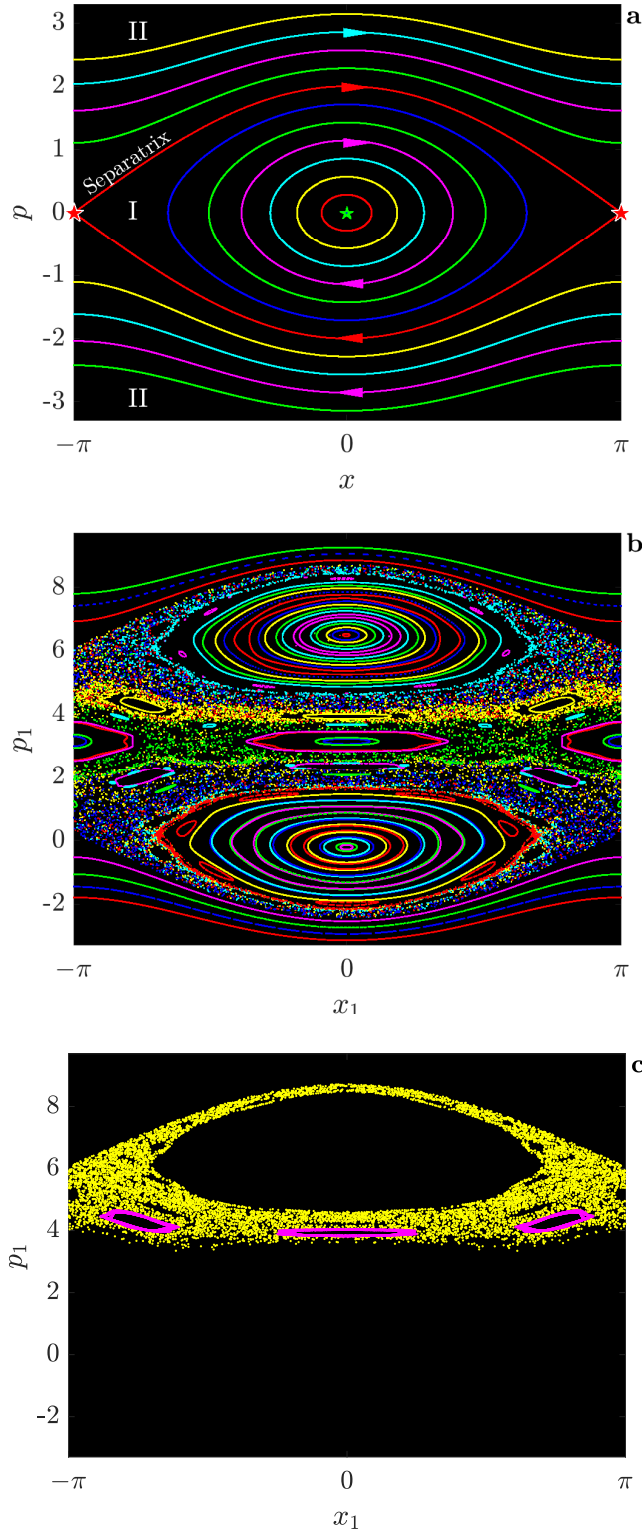


Figure 7: (a) Phase diagram (x = position/angle, p = momentum) of the simple rigid pendulum (units normalized). Green/red stars: stable/unstable fixed points (modulo 2π). Color coding indicates phase space trajectories for each set of initial conditions (x^0, p^0) , $N = 16$, from which the equations of motion are numerically integrated. (b) Poincaré section (aka surface of section) of the driven rigid pendulum ($N = 64$ initial conditions) (simplified Hamiltonian, see Chapter 6, [Morbidei, 2002](#)). (c) Same as (b) for $N = 2$, p_1^0 differs by 10^{-6} .

regime I will lead to libration, whereas starting at neighboring points in regime II will lead to rotation. However, for (x^0, p^0) very close to the separatrix, neighboring starting points may

lead to fundamentally different outcomes governing their motion, e.g., libration or rotation. In chaotic systems, one may think of the separatrix as “the cradle of chaos” (Murray and Holman, 2001).

While the motion of the simple rigid pendulum is non-chaotic (universally), this is not the case for the driven rigid pendulum (Fig. 7b). Imagine a driven pendulum by, for instance, applying a periodic force (torque) to the pendulum or periodically moving its pivot point, which results in the interaction of two oscillators (pendulum and pivot). Instead of two phase-space variables for the simple rigid pendulum, four variables are now needed to describe the motion, say x_1, p_1, x_2 and p_2 . Thus, the phase space is four-dimensional (4D), which cannot be fully represented in 2D. To visualize the dynamics, a lower-dimensional phase diagram is often constructed, called a Poincaré section, or surface of section. For example, for the driven pendulum, one may select the surface (x_1, p_1) , with x_2 perpendicular to the surface, and plot (x_1, p_1) only when $x_2 = 0$, i.e., at times when the phase trajectory intersects the (x_1, p_1) plane (see Fig. 7b). Usually, an additional condition is specified for p_2 , e.g., $p_2 > 0$. One can think of a Poincaré section as a stroboscopic image of the trajectory’s time evolution in phase space (Morbidielli, 2002).

The critical ingredient for chaotic dynamics are overlapping resonances. For illustration, consider the single resonance (Fig. 7a, one ‘cat’s eye’) and the two resonances (Fig. 7b, two ‘cat’s eyes’ atop one another). For certain parameter values of the driven pendulum (e.g., driving frequency close to the natural pendulum frequency), the two resonances are close enough to overlap (Fig. 7b, around $p_1 = \pi$). The structures of certain phase space regions still appear relatively simple, such as in the vicinity of the resonances centered at $(0,0)$ and $(0, \sim 2\pi)$ and for large $|p_1|$, corresponding to regimes I and II, respectively (Fig. 7a). The motion in these regions may be restricted to invariant (stable) tori, or KAM tori³ (for summary, see Morbidielli, 2002). However, for certain initial conditions, chaotic phase space regions appear, expressed in the Poincaré section as disordered sets of scattered points (see, e.g., transition areas between regions of libration and rotation, Fig. 7b and c). In chaotic regions of the phase space, nearby trajectories diverge exponentially, characterized by their Lyapunov exponent (see Section 1). As a result, the system is sensitive to small differences in initial conditions and small perturbations. For example, two trajectories of the driven pendulum $(x_1^0, p_1^0) = (0, \sim 3.82)$ that initially differ by only 10^{-6} in p_1^0 rapidly diverge and occupy different (separate) regions of the phase space (Fig. 7c). Prediction becomes impossible, as Poincaré had pointed out.

The driven pendulum serves as a useful illustration for various properties of chaotic systems, including the sensitivity to initial conditions. The full orbital dynamics of, for instance, the solar system, are of course substantially more complex (see below). Nevertheless, key elements such as the sensitivity to initial conditions and the overlap of resonances are also critical in solar system dynamics (note that for secular resonances, the g and s frequencies are involved, see Section 2.1.3). For example, it was recently discovered that Earth’s long eccentricity cycle can become unstable on long time scales due to the resonance

³KAM refers to the Kolmogorov-Arnold-Moser theorem, demonstrating the persistence of quasi-periodic motion on invariant tori (singular: torus) under small perturbations of, e.g., Hamiltonian systems (Kolmogorov, 1954; Arnold, 1963; Moser, 1962).

$$(g_1 - g_2) + (s_1 - s_2) \simeq 0 \text{ (see Zeebe and Lantink, 2024a)}$$

2.3.2. Solar System: Time Scales and Limitations

As mentioned above, large-scale dynamical chaos is an inherent property of the solar system, which has been independently confirmed in various numerical studies (e.g., Sussman and Wisdom, 1988; Laskar, 1989; Ito and Tanikawa, 2002; Morbidelli, 2002; Varadi et al., 2003; Batygin and Laughlin, 2008; Zeebe, 2015; Brown and Rein, 2020; Hernandez et al., 2022; Abbot et al., 2023; Zeebe and Lantink, 2024a). For observational studies, see, e.g., Ma et al. (2017); Westerhold et al. (2017); Olsen et al. (2019); Zeebe and Lourens (2019). Dynamical chaos affects the secular frequencies g_i and s_i (see Section 2.1.3), where the terms $(g_4 - g_3)$ and $(s_4 - s_3)$, for instance, show chaotic behavior already on a 50-Myr time scale. As a result, astronomical solutions diverge around $t = \pm 50$ Myr, which fundamentally prevents identifying a unique solution on time scales $\gtrsim 10^8$ y (Laskar et al., 2004; Zeebe, 2017; Zeebe and Lourens, 2019). The quest for a single deterministic solution, which conclusively describes the solar system’s evolution for all times (in the spirit of Laplace’s demon, see Laplace, 1951), must therefore be regarded as quixotic. In fact, long-term predictability is fundamentally unachievable (Poincaré, 1914). The chaos not only severely limits our understanding and ability to reconstruct and predict the solar system’s history and long-term future, it also imposes fundamental limits on geological and astrochronological applications such as developing a fully calibrated astronomical time scale beyond ~ 50 Ma, including the SEC (for recent efforts, see Zeebe and Lourens, 2019, 2022b; Kocken and Zeebe, 2024).

The limits imposed by dynamical chaos on astronomical calculations may be illustrated by comparing Earth’s eccentricity (e_\oplus) from different OS prior to -50 Myr (Fig. 8). As an example, we select three of the most current and up-to-date OS (ZB18a, ZB20a, and ZB20b), which have been constrained by geologic data up to an age of 66 Ma (see Section 2.5 and Zeebe and Lourens (2019, 2022b)). ZB18a, ZB20a, and ZB20b use identical initial conditions but feature slightly different J_2 values (for details, see Section 2.6 and Zeebe, 2017; Zeebe and Lourens, 2019, 2022b) and number of asteroids included in the simulation. Visually, e_\oplus calculated based on these three OS is nearly identical back to ca. -58 Myr but diverge quickly beyond that time, as highlighted by a 2.4-Myr filter (Fig. 8). The 2.4-Myr filter is sensitive to the amplitude modulation of eccentricity, aka very long eccentricity nodes (VLN), with frequency $(g_4 - g_3)$. Of the La10x solutions, La10b and La10c appear to provide the best match with geological data to ~ 58 Ma, but not beyond (Westerhold et al., 2017; Zeebe and Lourens, 2019, 2022b). La10b, for example, exhibits a large 100-kyr amplitude just prior to -59 Myr (see Fig. 8), while ZB18a and ZB20a exhibit small 100-kyr amplitudes (VLNs). Features such as VLNs are important criteria to distinguish between different OSs based on geologic data (Westerhold et al., 2017; Zeebe and Lourens, 2019, 2022b).

The example using e_\oplus based on different OSs (Fig. 8) again illustrates one key feature of dynamical chaos, i.e., the sensitivity to tiny perturbations or small differences in initial conditions (see Section 2.3.1). For example, the masses of the largest asteroids are roughly *ten billion times smaller* than the solar mass (which represents the magnitude of the first-order gravitational interaction). Yet, changing the number of asteroids included in the simulation drives the solutions apart beyond ca. -58 Myr (Fig. 8). Small differences in trajectories grow exponentially, with a time constant (Lyapunov time, see Section 1) for the inner planets of

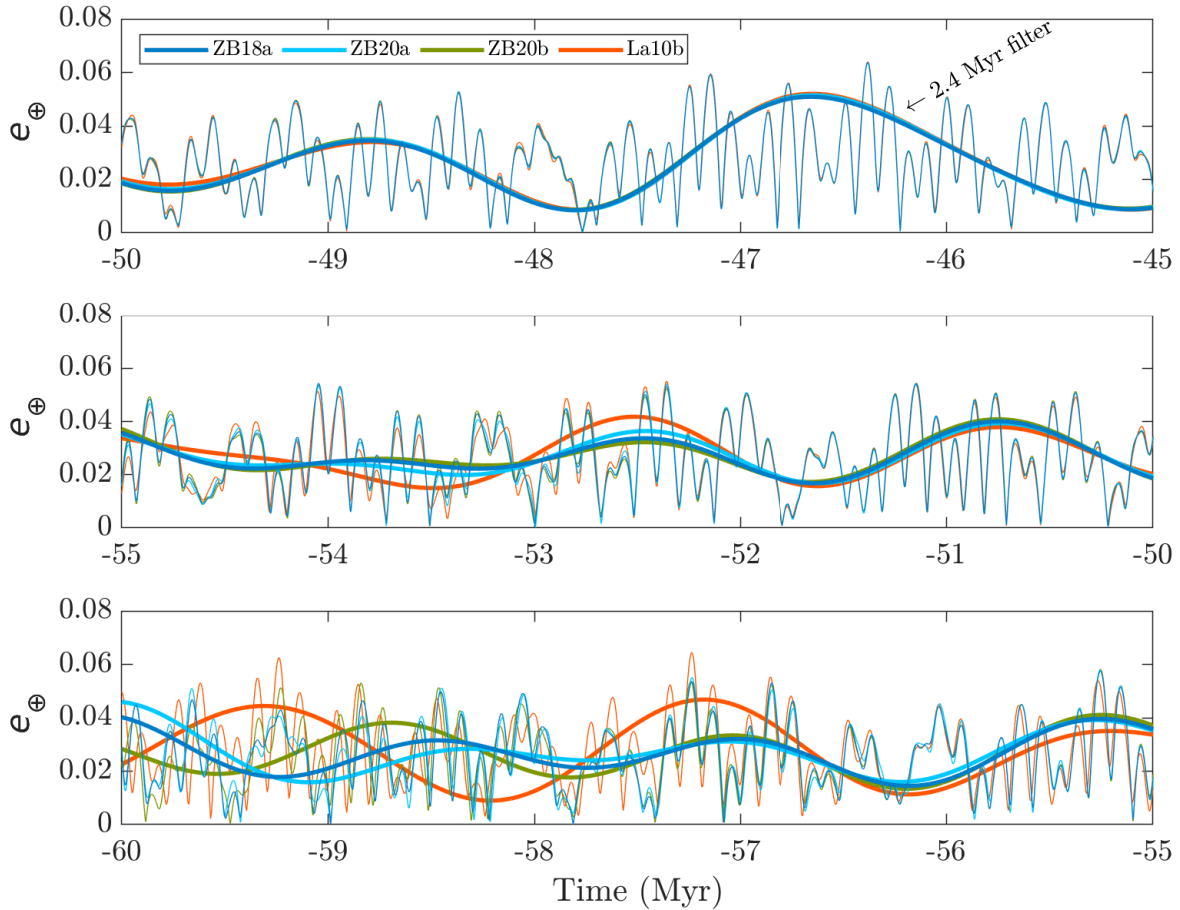


Figure 8: Earth’s orbital eccentricity (e_{\oplus}) from different OS: ZB18a (Zeebe and Lourens, 2019), ZB20a and ZB20b (Zeebe and Lourens, 2022b), and La10b (Laskar et al., 2011). The 2.4-Myr filter is sensitive to the amplitude modulation of eccentricity, with minima corresponding to a reduced amplitude of the short eccentricity cycle, aka very long eccentricity nodes (VLN).

$\sim 3\text{--}5$ Myr estimated numerically (Laskar, 1989; Varadi et al., 2003; Batygin and Laughlin, 2008; Zeebe, 2015). For example, a difference in initial position of 1 cm grows to ~ 1 AU ($= 1.496 \times 10^{11}$ m) after 90–150 Myr, which makes it fundamentally impossible to predict the evolution of planetary orbits accurately beyond a certain time horizon.

In contrast to the limitations discussed above (largely due to unstable terms such as $(g_4 - g_3)$ and $(s_4 - s_3)$), another frequency term appears more promising as it shows more stable behavior. For example, it has hitherto been assumed that $(g_2 - g_5)$ was practically stable in the past and has been suggested for use as a “metronome” in deep-time geological applications, i.e., far exceeding 50 Ma (Laskar et al., 2004; Kent et al., 2018; Spalding et al., 2018; Meyers and Malinverno, 2018; Montenari, 2018; Lantink et al., 2019; De Vleeschouwer et al., 2024). The $(g_2 - g_5)$ cycle, which is the dominant term in Earth’s orbital eccentricity in the recent past (~ 405 kyr, see Fig. 6) may thus have been regarded as an island of stability in a sea of chaos. However, as mentioned above, $(g_2 - g_5)$ can also become unstable over long time scales (Zeebe and Lantink, 2024a).

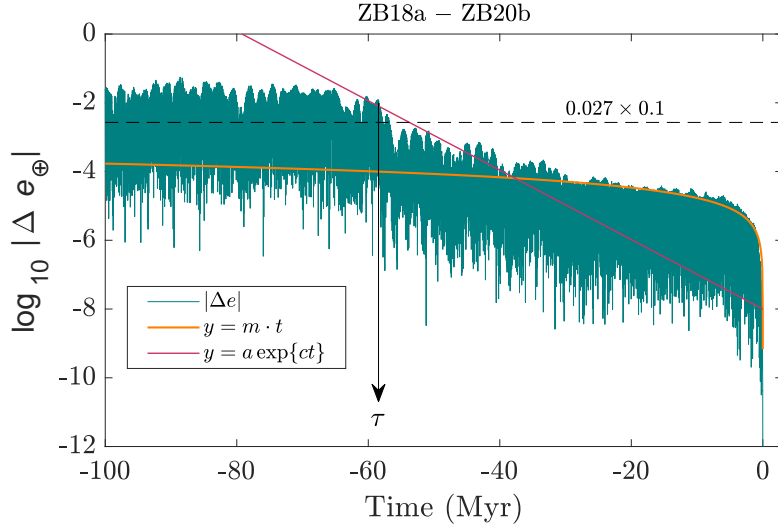


Figure 9: Difference in Earth’s orbital eccentricity on a log- y scale, $\log_{10} |\Delta e_{\oplus}|$, between the solutions ZB18a and ZB20b over the past 100 Myr. The arrow indicates the divergence time τ , when $\max|\Delta e_{\oplus}|$ irreversibly crosses $\sim 10\%$ of mean e_{\oplus} ($\sim 0.027 \times 0.1$, dashed horizontal line). Orange curve: simple fit function with linear growth in $|\Delta e_{\oplus}|$. Red line: exponential growth in $|\Delta e_{\oplus}|$ (linear on log- y scale) with a Lyapunov time of 4.3 Myr (see text).

2.3.3. Divergence Time τ

The action of chaos on Earth’s orbital evolution may be illustrated by the difference between two eccentricity solutions ($|\Delta e_{\oplus}|$), say plotted on a log scale (Fig. 9). Starting at t_0 and integrating backwards in time, integration errors dominate initially. Integration errors usually grow polynomially (for angle-like variables), here $\propto t$ and dominant for $t \gtrsim -40$ Myr (see orange line, Fig. 9; note that a function linear in t appears non-linear on a log scale). Ultimately, the divergence of trajectories is dominated by exponential growth ($t \lesssim -40$ Myr), which is indicative of chaotic behavior (red line, Fig. 9). For $t \lesssim -60$ Myr, the solutions have completely diverged and their difference may reach the maximum of ~ 0.06 ($\max |\Delta e_{\oplus}|$ no longer increases, see Fig. 8). The difference between two orbital solutions may be tracked by the divergence time τ , i.e., the time interval after which the absolute difference in Earth’s eccentricity ($|\Delta e_{\oplus}|$) irreversibly crosses $\sim 10\%$ of mean e_{\oplus} ($\sim 0.027 \times 0.1$, Fig. 9). Simply put, τ represents the time interval beyond which the solutions no longer agree. The divergence time is largely controlled by the Lyapunov time, although the two are different quantities.

2.3.4. Chaos and Inapplicability of Basic Statistics

Chaos introduces elements of inherent unpredictability into dynamical systems, which generally leads to fundamental unaccountability in terms of basic statistics. Note that the following is not a criticism of statistics, but rather of attempts to apply basic statistical concepts to chaotic patterns, which may arise from a misunderstanding of the dynamics of the system. For instance, consider a dynamical system parameter, which, when increased by a small amount δ produces a change in a system variable by an amount X . If δ is now varied incrementally, one may expect that X is a function of δ (linear or nonlinear) that somehow scales with the size of δ . However, this is generally not the case in chaotic systems (see Section 2.3.1). As an example, consider the solar system in which Earth’s initial position (x -coordinate) is varied by $\delta = \Delta x_0$. The system is then integrated for different Δx_0 over 100 Myr and the differences in Earth’s orbital eccentricity e_{\oplus} are evaluated (Zeebe, 2023), say

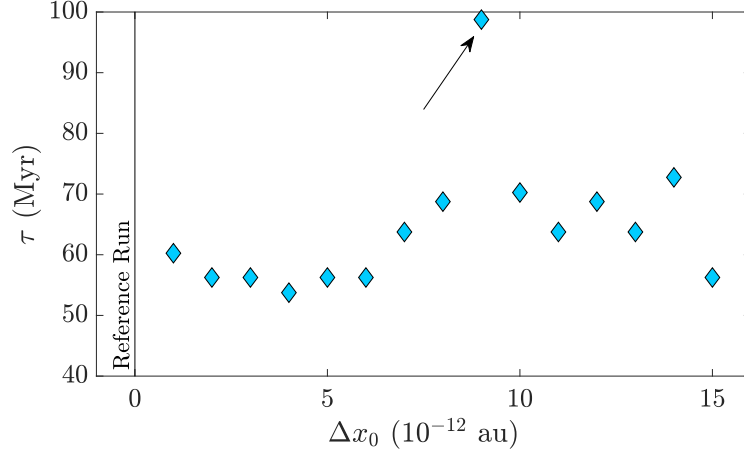


Figure 10: Ensemble integrations with `orbitN` (general relativity, J_2 , and the lunar contribution turned off, see Zeebe, 2023). Earth’s initial x -coordinate is perturbed by a small $\Delta x_0 = 1 \times 10^{-12}$ au (~ 15 cm), relative to the corresponding reference run ($\Delta x_0 = 0$ au). The difference between two orbital solutions i and j may be tracked using the divergence time τ (see Fig. 9 and Zeebe, 2017). The run resulting in the largest $\tau \simeq 100$ Myr (arrow) is not a mistake, numerical error, or “outlier” (see text).

tracked using the divergence time τ (see Fig. 10). Note that τ is not a measure of accuracy or inaccuracy.

First, there is no systematic relationship between τ and Δx_0 that somehow scales with the size of Δx_0 . Second, the run resulting in the largest $\tau \simeq 100$ Myr (see arrow) is not a mistake, numerical error, or “outlier” that can therefore be excluded (the run was carefully examined). The run is a proper solution of the system, illustrating the unpredictability and unaccountability of chaotic systems in terms of basic statistics. For example, values that fall outside two or three sigma from the mean are often considered outliers, which is not applicable here. One important corollary is that it is generally not possible to “tune” or “fit” astronomical solutions to geological data. The best that can probably be done is to “constrain” astronomical solutions by geological data. In other words, to create large ensembles of solutions via parameter variations and select/discard those solutions that show good/poor agreement with the data (Zeebe and Lourens, 2019, 2022b).

As outlined in the preceding sections, solar system chaos is key to understanding the limitations imposed on orbital solutions by chaotic dynamics, resonances, the behavior of ensemble integrations, and more. Chaos also causes critical changes in the amplitude modulation of orbital forcing signals, which, if expressed in cyclostratigraphic sequences, can be used to reconstruct the solar system’s chaotic history. Elements of amplitude (and frequency) modulation are covered in Section 2.4.

2.4. Amplitude & Frequency Modulation (AM & FM)

Amplitude and frequency modulation of orbital forcing signals is similar to AM/FM techniques used in radio broadcasting. Schematically, the carrier signal (high frequency) is modulated, resulting either in slow modulation of the amplitude (AM) or frequency (FM), see Fig. 11. For example, the astronomical carrier frequency may be precession, eccentricity, or obliquity, while the AM frequency (or “beat”, see below) may be eccentricity or various combinations of $(g_i - g_j)$ and $(s_i - s_j)$, see Section 2.1.4. As described below, frequency modulation is less commonly used than amplitude modulation in astrochronology and cyclostratigraphy.

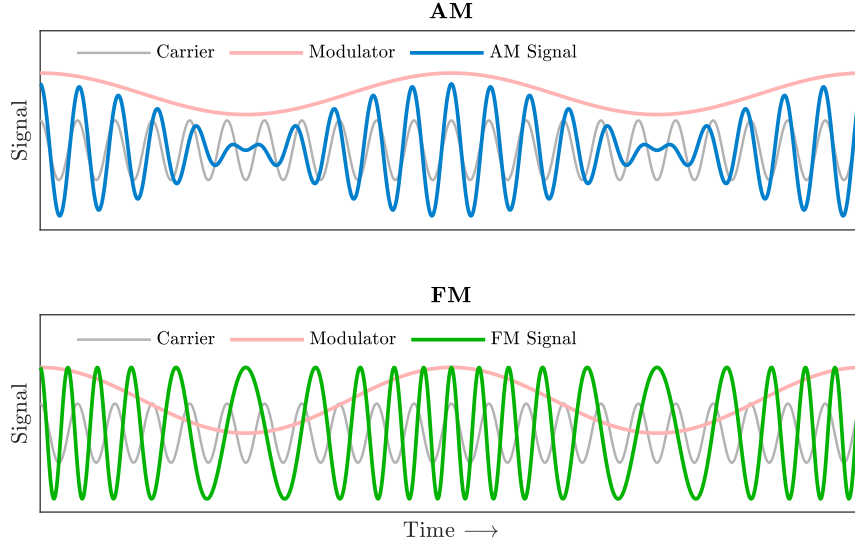


Figure 11: Schematic illustration of amplitude & frequency modulation (AM & FM).

Also, while there is a direct analogy between radio AM and astronomical forcing AM, the analogy is not straightforward for the FM case study discussed here (Section 2.4.2).

2.4.1. AM

Amplitude modulation is frequently used in cyclostratigraphy because AM cycles are often expressed in geologic sequences (also called “beats” in analogy to beat frequencies in music). For example, the amplitude of climatic precession is modulated by eccentricity (in a very simple manner, i.e., eccentricity is the envelope of climatic precession, $\bar{p} = e \sin \bar{\omega}$, see Fig. 1). Also, the SEC’s amplitude is modulated by the LEC. Bundles of four SECs in the recent past (each ~ 100 kyr, for details see Eq. (6)) represent one LEC (405 kyr, see Fig. 13a). On even longer time scales, the eccentricity amplitude is modulated by $(g_4 - g_3)$, which leads to very long eccentricity nodes (VLNs) with much reduced SEC amplitude and a recent period of ~ 2.4 Myr (Fig. 12a). The spectrum of Earth’s orbital eccentricity is largely dominated by simple combinations of the g frequencies g_2 to g_5 (see Tables 3 and 4). Thus, there is a simple relationship between, for instance, $(g_4 - g_3)$ and the other relevant $(g_i - g_j)$ terms (individual SEC’s are $\sim 124, 131, 95$, and 99 kyr):

$$\begin{aligned}
 (g_4 - g_3)^{-1} &= (1/72.328 - 1/74.613)^{-1} = 2362 \text{ kyr} \\
 &= (g_{42} - g_{32})^{-1} = (g_{45} - g_{35})^{-1} \\
 &\simeq (1/123.87 - 1/130.73)^{-1} \simeq (1/94.87 - 1/98.84)^{-1} .
 \end{aligned} \tag{6}$$

Importantly, owing to chaotic dynamical behavior, the fundamental frequencies (and hence the beats) are not constant, but change over time. The changing VLN patterns beyond about 50 Ma observed in cyclostratigraphic records are important criteria to distinguish between different orbital solution (Westerhold et al., 2017; Zeebe and Lourens, 2019, 2022b).

As discussed above, there is no direct analogy between eccentricity and inclination (see Section 2.1.2). Similarly, the analogy between their amplitude modulations (i.e., between $(g_i - g_j)$ terms and $(s_i - s_j)$ terms) is limited as well. The orbital parameter closely related to inclination is obliquity, which is often expressed in cyclostratigraphic sequences. Thus, to

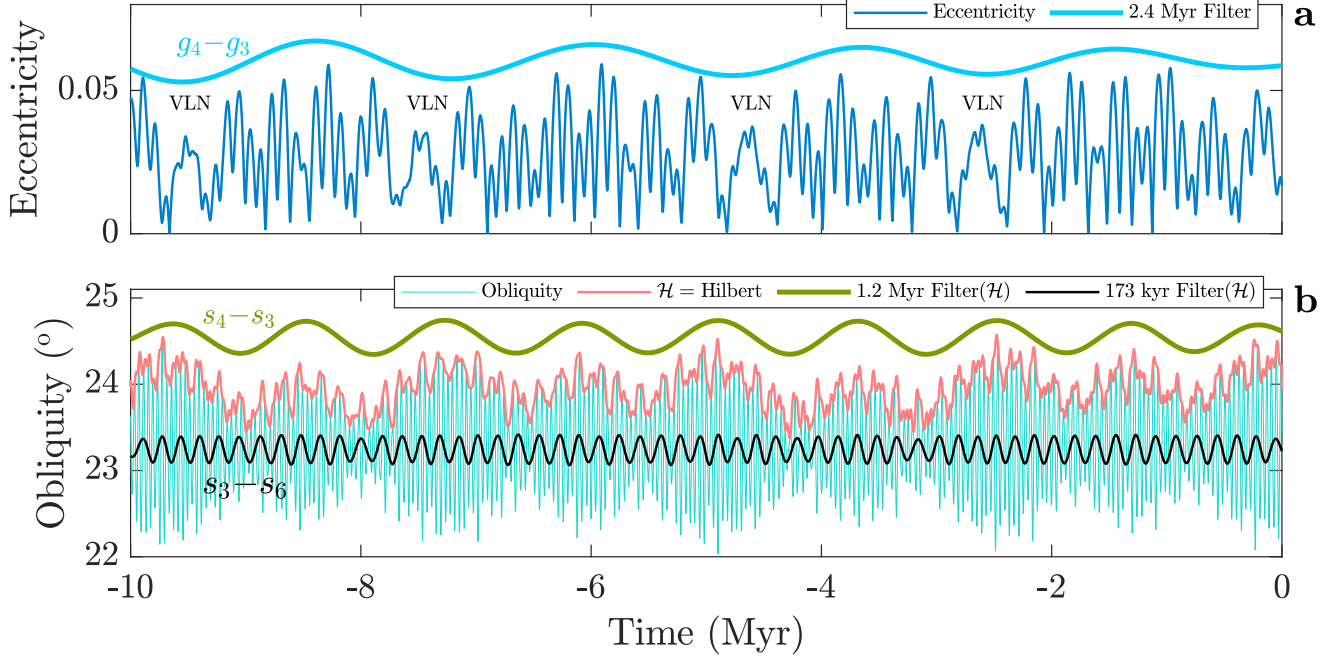


Figure 12: (a) Earth's orbital eccentricity and ~ 2.4 Myr filter corresponding to $(g_4 - g_3)$. VLN = very long eccentricity node. Filters are plotted using arbitrary amplitudes and vertical offsets. (b) Obliquity, its Hilbert transform $\mathcal{H}(\epsilon)$, ~ 1.2 Myr filter of $\mathcal{H}(\epsilon)$ corresponding to $(s_4 - s_3)$, and 173 kyr filter of $\mathcal{H}(\epsilon)$ corresponding to $(s_3 - s_6)$.

examine the AM associated with $(s_i - s_j)$ terms, it is helpful to examine the AM of obliquity (see Fig. 12b). Again, to do so, we first extract the envelope of obliquity by applying the Hilbert transform, $\mathcal{H}(\epsilon)$. The two largest peaks in $\mathcal{H}(\epsilon)$'s spectrum are located at periods of ~ 1.2 Myr and ~ 173 kyr (see Fig. 6). The 1.2-Myr period corresponds to $(s_4 - s_3)$, which is currently in a 2:1 resonance with $(g_4 - g_3)$ (Section 2.1.4). On time scales beyond ~ 50 Myr, the $(s_4 - s_3):(g_4 - g_3)$ ratio is subject to chaotic transitions and may exhibit a wide range of values on Gyr-time scale (Zeebe and Lantink, 2024b). The 173-kyr period corresponds to $(s_3 - s_6)$, which is significant in the recent past (e.g., Shackleton et al., 1999; Hinnov, 2000; Pälike et al., 2004), and has been suggested to be expressed in multiple proxy records of Mesozoic and Cenozoic age (for recent summary see, e.g., Huang et al., 2021). However, for records older than ~ 50 Ma, the assumed assignment and period is ambiguous and hence problematic owing to the lack of generally stable and prominent metronomes or geochronometers, including $(s_3 - s_6)$ (see Section 2.2).

2.4.2. FM

Frequency modulation is less commonly used than amplitude modulation in cyclostratigraphic studies (for a few examples, see Herbert, 1992; Liu, 1995; Hinnov and Park, 1998; Rial, 1999; Hinnov, 2000; Zeeden et al., 2015; Laurin et al., 2016; Piedrahita et al., 2022). One major challenge for cyclostratigraphic applications is the conversion from stratigraphic depth to time. Variations in sedimentation rate that are not taken into account would perturb the frequency of recorded astronomical cycles (similar to the FM illustration shown in Fig. 11). Conversely, tuning of the stratigraphic record to an astronomical frequency would map any frequency modulation in the data to variations in sedimentation rate. These issues represent substantial obstacles to FM analyses of sedimentary data. Another potentially complicating

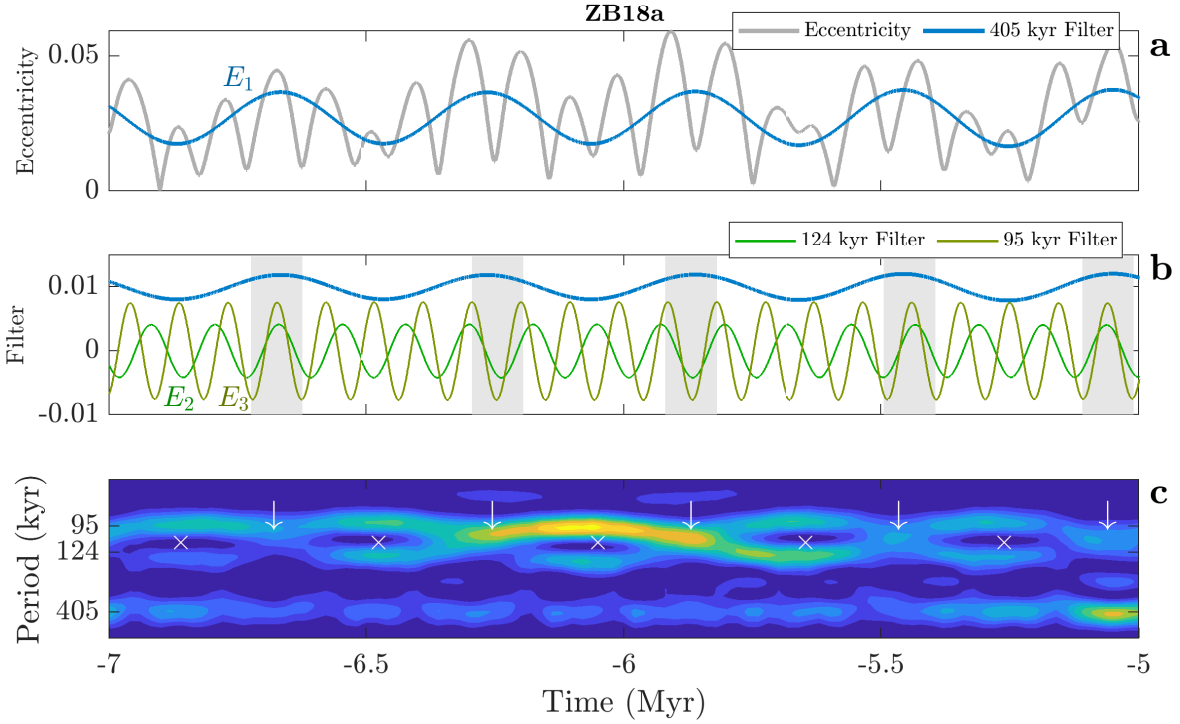


Figure 13: Illustration of eccentricity-related FM interference patterns. (a) Earth’s orbital eccentricity (e_{\oplus}) from solution ZB18a and 405-kyr filter (E_1). (b) Narrow filters of e_{\oplus} around 124 (E_2) and 95 kyr (E_3). Gray bars mark intervals of E_2 - E_3 constructive (in-phase) interference. Blue: scaled and offset 405-kyr filter from (a). (c) Evolutive Harmonic Analysis (EHA) of e_{\oplus} (showing amplitude, not spectral power) using *astrochron* (Meyers, 2014). Arrows and crosses: nodes and rings in E_2 - E_3 amplitude corresponding to maxima and minima in E_1 , respectively (see (a)).

factor regarding FM is that age-model tuning approaches may introduce systematic frequency modulations (e.g., Zeeden et al., 2015). Nevertheless, analysis of short eccentricity-related FM interference patterns in stratigraphic sequences can, for instance, be used to discern LEC minima and maxima from SEC records (e.g., Laurin et al., 2016; Piedrahita et al., 2022). The link between the LEC and SECs is of course due to the relationship between the g frequencies and their involvement in Earth’s orbital eccentricity, e_{\oplus} (see Sections 2.1.3 and 2.1.4). The strongest terms in e_{\oplus} ’s spectrum in the recent past are the LEC (g_2 – g_5) (~ 405 kyr) and the SECs (g_4 – g_2) and (g_4 – g_5) (~ 124 and 95 kyr, E_2 and E_3 for short) (see Figs. 6 and 13). The combination of the two SECs in turn yields the LEC (E_1):

$$(1/95 - 1/124)^{-1} \simeq 405 \text{ kyr} . \quad (7)$$

Narrow filters of e_{\oplus} around 124 and 95 kyr show interference patterns that correlate with minima and maxima in E_1 . For instance, E_2 and E_3 interfere constructively (in-phase) during E_1 maxima and destructively (out-of-phase) during E_1 minima (Fig. 13a and b). Note that LEC maxima and minima correlate with large and small SEC amplitudes, respectively. Evolutive Harmonic Analysis (EHA) of e_{\oplus} reveals a chain pattern in the E_2 - E_3 amplitude, where nodes (single amplitude and period) correspond to E_1 maxima and rings (split amplitudes and periods) to E_1 minima (see arrows and crosses, Fig. 13c). Thus, the SEC-FM interference patterns can be used to deduce LEC minima and maxima (Laurin et al., 2016).

2.5. Up-to-Date Orbital Solutions

As described above, there is a long history of OSs — yet only a few are up-to-date and should be employed in current and future applications, which has not been the case in many

Table 5: Selected (recent or frequently used) orbital solutions.

Label	Time Span Provided (Myr)	Time Span Valid (Myr) ^a	Reference	Notes
ZB23x	−3500 to 0	−48 to 0	Zeebe and Lantink (2024b)	^b
ZB20x	−300 to 0	−66 to 0	Zeebe and Lourens (2022b)	^c
ZB18a	−300 to 0	−66 to 0	Zeebe and Lourens (2019, 2022b)	^c
ZB17x	−100 to 0	−50 to 0	Zeebe (2017)	
La10x	−250 to 0	−50 to 0	Laskar et al. (2011)	
La04	−250 to 250	−40 to 0	Laskar et al. (2004)	^d

^a Approximate valid time span.

^b Ensemble solutions designed for deep-time applications. For −300 to 0 Myr, ZB18a and ZB20x are recommended.

^c Valid time span indicates geologically constrained time span.

^d Outdated compared to La10x, ZB17x, ZB18a, and ZB20x (see text).

recent applications, indicating confusion about proper use of OSs (see remark at the end of this section). For the time span from −300 to 0 Myr, we recommend the solutions ZB18a and ZB20x, which have been constrained by geologic data up to an age of 66 Ma (see Table 5). Importantly, significantly beyond the geologically constrained intervals, or the solution’s validity range, the OSs are unconstrained owing to solar system chaos. For much older time intervals, the OSs may serve as examples for possible dynamical patterns ([Zeebe and Lantink, 2024a,b](#)), or as potential tuning targets for the LEC in the recent past (~405 kyr). However, the probability that a particular OS represents the actual, unique history of the solar system is near zero significantly beyond the OS’s validity range. For example, at double-precision floating-point arithmetic, one could generate 10^{21} possible different solutions, all within observational uncertainties just for Earth’s position (ignoring all other physical and numerical uncertainties in solar system models, initial conditions, etc., see [Zeebe, 2017](#)). Regarding geological constraints on OSs based on data-OS comparisons ([Zeebe and Lourens, 2019](#)), note that a bad match in a well-constrained younger interval disqualifies a solution for *all* older intervals ([Zeebe and Lourens, 2022b](#)).

The solutions La10x, ZB17x, ZB18a, and ZB20x agree closely to about −50 Myr. However, the La04 solution does not and is only valid to about −40 Myr ([Zeebe, 2017](#); [Laskar, 2020](#)). The physical model underlying the La04 solution did not include asteroids and used initial conditions from the DE406 ephemeris (an older ephemeris version created in 1997, see [Standish, 1998](#)). Given the above and that La04 disagrees beyond −40 Myr with the updated solutions La10x from the same group, La04 is considered outdated. Thus, it is clear at this point that La04 does not represent a proper solution of the solar system beyond its valid time span and should no longer be considered for any time prior to ca. −40 Myr. The situation is different (i.e., the jury is still out) for e.g., ZB18a and ZB20x, which have not shown inconsistencies with updated/more recent solutions or geologic data ([Zeebe and Lourens, 2022b](#)). In other words, ZB18a and ZB20x could theoretically be viable solutions beyond their valid time span, whereas La04 can not. Unfortunately, there is substantial confusion in the literature

regarding the valid time span of astronomical solutions, most notably La04 (of the numerous examples only a few recent ones are cited here, e.g., [Liu et al., 2019](#); [Husinec and Read, 2023](#); [Wu et al., 2023](#); [Charbonnier et al., 2023](#); [Dutkiewicz et al., 2024](#); [Vervoort et al., 2024](#)).

2.6. Additional Physical/Dynamical Effects in Up-to-Date Orbital Solutions

Generating adequate, state-of-the-art orbital solutions requires accurate and fast integration of the fundamental dynamical equations for the main solar system bodies (see Section 1). Furthermore, several additional effects need to be considered, some (or all) of which have been included in fully numerical solutions (e.g., [Quinn et al., 1991](#); [Varadi et al., 2003](#); [Laskar et al., 2004](#); [Laskar et al., 2011](#); [Zeebe, 2017, 2023](#)). Additional effects include: (1) post-Newtonian corrections from general relativity (1PN = first-order post-Newtonian), (2) the effect of the Moon, (3) the Sun’s quadrupole moment J_2 , and (4) a contribution from asteroids. 1PN effects are critical (non-negligible, [Einstein, 1916](#)) and a fast (symplectic) implementation is highly desirable for long-term integrations (see discussion in [Saha and Tremaine, 1994](#); [Zeebe, 2023](#)). The Moon may be included as a separate object ([Varadi et al., 2003](#); [Rauch and Hamilton, 2002](#); [Laskar et al., 2004](#); [Zeebe, 2017](#)), or the Earth-Moon system may be modeled as a gravitational quadrupole ([Quinn et al., 1991](#); [Varadi et al., 2003](#); [Rauch and Hamilton, 2002](#); [Zeebe, 2017, 2023](#)). The solar quadrupole moment J_2 is due to the rotation of the Sun, which causes solar oblateness and slightly distorts the gravitational field and hence the planetary orbits (for summary, see, e.g., [Rozelot and Damiani, 2011](#)). Despite their comparatively small mass, asteroids are dynamically relevant and have been included in short-term, as well as long-term integrations (e.g., [Standish et al., 1995](#); [Laskar et al., 2011](#); [Zeebe, 2017](#); [Antoñana et al., 2022](#)). Note that while the effects from J_2 and asteroids may appear negligible, their contributions become critical for astronomical solutions over, e.g., 50-Myr time scale due to solar system chaos (Section 2.3). The effect of solar mass loss over 50 Myr may be neglected ([Zeebe and Lourens, 2019](#)) but needs to be considered in deep time (e.g., [Minton and Malhotra, 2007](#); [Spalding et al., 2018](#); [Zeebe and Lantink, 2024a](#)).

3. Precession-Tilt Solutions

The second type of astronomical solutions discussed here (in addition to orbital solutions), are Precession-Tilt (PT) solutions. As mentioned above, precession and tilt (= obliquity) are among the most frequently used orbital parameters in the Earth sciences (see Fig. 1). Defining obliquity (ϵ) is straightforward, that is, ϵ is the angle between Earth’s spin axis and the orbit normal, i.e., unit vectors \mathbf{s} and \mathbf{n} , where \mathbf{n} is perpendicular to Earth’s orbital plane = ecliptic (see Fig. 14). Equivalently, obliquity is the angle between the celestial equator and the ecliptic. In contrast, the term *precession* may be used interchangeably in the literature for different concepts/motions. Moreover, the geometric description, as well as the different notations and symbols used by different authors, is often confusing. Importantly, however, an accurate description of precession is inevitably somewhat more complex because of the various motions and angles involved. Most critical for cyclostratigraphic and astrochronological applications is being aware of the differences between climatic and luni-solar precession, as well as nodal and apsidal precession (Section 2.1.3).

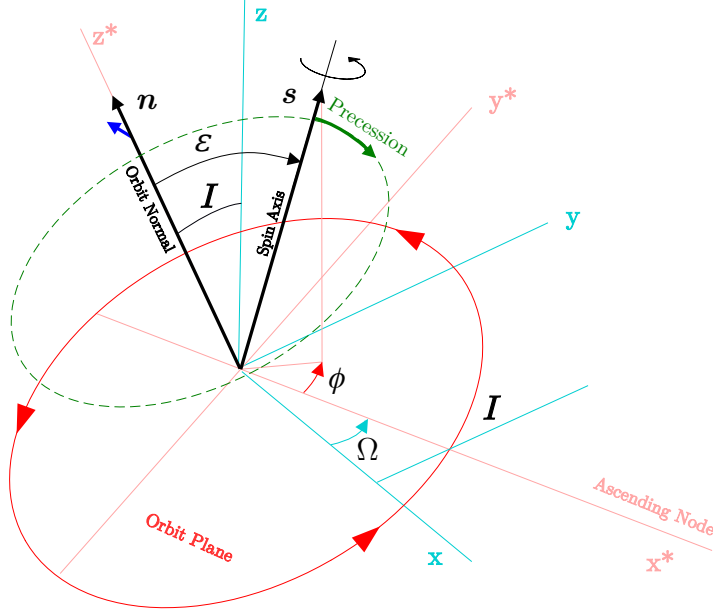


Figure 14: Inertial (fixed) coordinate system $(x, y, z, \text{light blue})$ and coordinate system moving with the orbit plane $(x^*, y^*, z^*, \text{red})$, with z^* parallel to the orbit normal \mathbf{n} and x^* along the ascending node. \mathbf{s} is the spin axis, the obliquity (axial tilt) ϵ is the angle between \mathbf{s} and \mathbf{n} ($\cos \epsilon = \mathbf{n} \cdot \mathbf{s}$). Ω is the longitude of the ascending node, I is the orbital inclination (angle between z^* and z), and ϕ measures the precession angle in the orbit plane (see text). \mathbf{s} slowly precesses westward (clockwise) along the ecliptic in the opposite direction (retrograde, green arrow and green dashed line) to Earth's orbital motion (red arrows) and spin. The planetary (or ecliptic) precession is indicated by the small blue arrow (see text).

3.1. Luni-Solar and Climatic Precession

At present, the Earth rotates on its axis at an angular velocity of $\sim 7.29 \times 10^{-5} \text{ rad s}^{-1}$ (see spin axis vector \mathbf{s} , Fig. 14). The spin axis itself slowly precesses westward (clockwise, precession angle ϕ , Fig. 14) along the ecliptic in the opposite direction (retrograde, green arrow) to Earth's orbital motion and spin (red arrows, see also Fig. 1). The axial precession (rate) along the fixed ecliptic with respect to space is referred to as *luni-solar precession* (Williams, 1994). The present precession rate of the total space motion at t_0 is $\Psi_0 \simeq 50.38'' \text{ y}^{-1}$ (Capitaine et al., 2003), corresponding to a period of $\sim 25.7 \text{ kyr}$ (Ψ represents a frequency, i.e., rate of change = time derivative, see Section 3.2; conventionally, Ψ is taken positive). Over time, the axial precession therefore causes a notable motion of the equinoxes westward along the ecliptic. When it comes to astronomical forcing of Earth's climate, however, it is not the position of the equinoxes relative to the fixed stars that matters (ϕ alone) but the position relative to Earth's elliptic orbit (see Section 1.1), i.e., the perihelion (for further illustrations, see, e.g., Hinnov, 2018; Lourens, 2021). In addition, the forcing depends on orbital eccentricity (in a circular orbit where $e = 0$, for example, the equinox position is inconsequential). Climate forcing is thus controlled by the *climatic precession* \bar{p} (see Fig. 1):

$$\bar{p} = e \sin \bar{\omega} , \quad (8)$$

where $\bar{\omega} = \varpi + |\phi|$ is the longitude of perihelion measured from the moving equinox (see below for ϕ 's sign; note also that various symbols are used for $\bar{\omega}$ in the literature). As a result, precessional climate forcing does not follow a simple sine function with 25.7-kyr periodicity

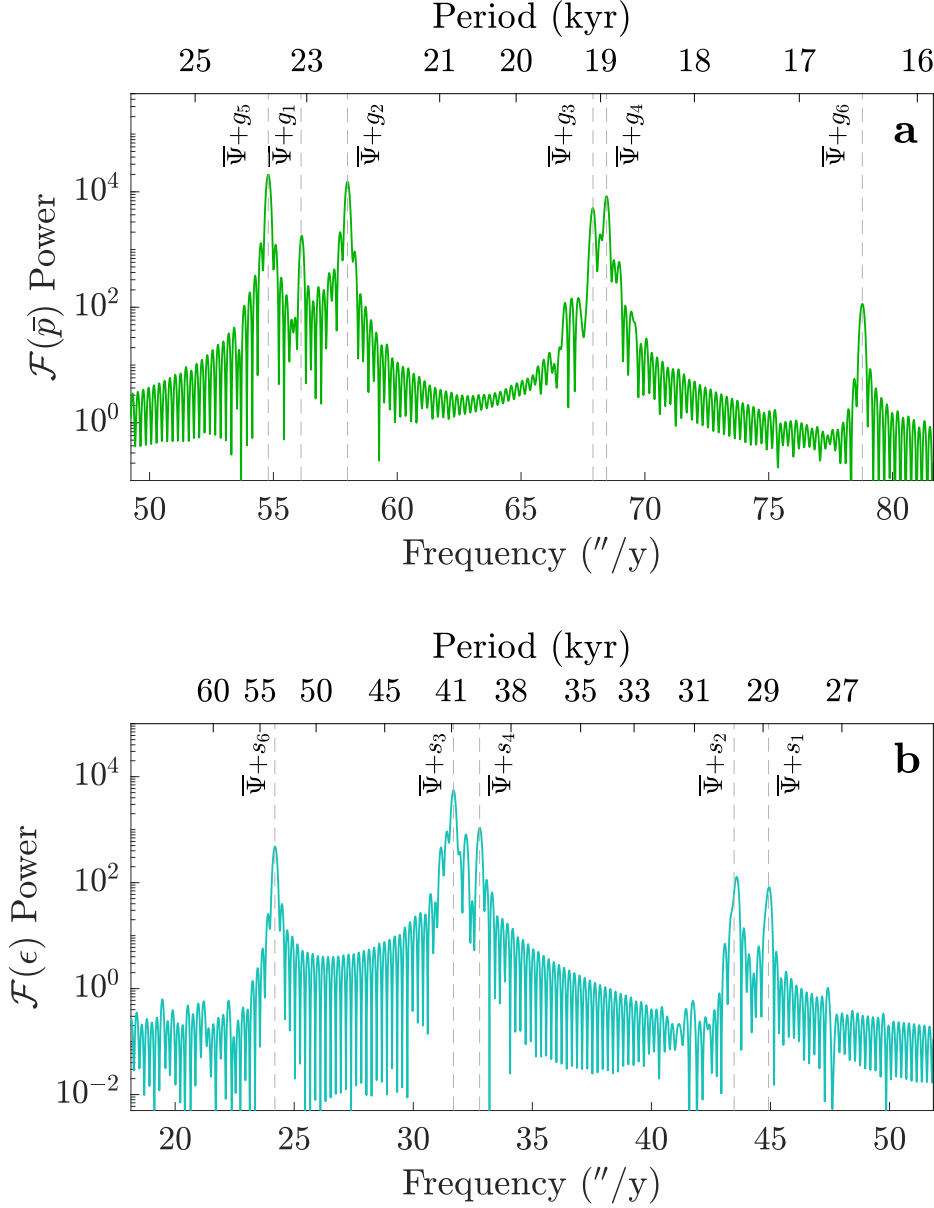


Figure 15: (a) FFT = $\mathcal{F}(\bar{p})$ of climatic precession ($\bar{p} = e \sin \bar{\omega}$) and (b) FFT = $\mathcal{F}(\epsilon)$ of obliquity, both from `snvec` output based on ZB18a(1,1) (see Section 3.3) over a 6-Myr interval (-6 to 0 Myr).

but depends on the frequency spectra of ϖ and ϕ , with its amplitude modulated by e (see Figs. 1 and 15).

Given that the precession rate is related to Ψ and ϖ 's rate is related to the g-mode frequencies g_i (see Section 2.1.3), one might expect that a spectral analysis of the climatic precession would show peaks at $\bar{\Psi} + g_i$, where $\bar{\Psi}$ is the mean Ψ across the analyzed interval. For retrograde axial precession and prograde apsidal precession, the frequencies add up to a higher frequency. Indeed \bar{p} 's power spectrum shows dominant peaks, for instance, at ~ 19 , ~ 22.4 , and ~ 23.7 kyr, corresponding to $\bar{\Psi} + g_i$ where $i = 3, 4, 2$ and 5 (Fig. 15). Analogous to $\bar{\Psi} + g_i$, which yields the precession frequencies, $\bar{\Psi} + s_i$ yields the obliquity frequencies. Note

Table 6: Frequencies (ordered by amplitude) of climatic precession (\bar{p}) and obliquity (ϵ).^a

Frequency	Value (" y ⁻¹)	Period (kyr)	Note
$\bar{\Psi} + g_5$	54.79	23.65	
$\bar{\Psi} + g_2$	57.99	22.35	
$\bar{\Psi} + g_4$	68.45	18.93	
$\bar{\Psi} + g_3$	67.90	19.09	
$\bar{\Psi} + g_1$	56.14	23.08	
$\bar{\Psi} + g_6$	78.78	16.45	
$\bar{\Psi} + s_3$	31.69	40.90	
$\bar{\Psi} + s_4$	32.79	39.52	
$\bar{\Psi} + s_3 + g_{43}$	32.21	40.23	^b
$\bar{\Psi} + s_6$	24.19	53.57	
$\bar{\Psi} + s_3 - g_{43}$	31.17	41.58	^b
$\bar{\Psi} + s_1$	44.94	28.84	

^a From FFT of **snvec** output based on ZB18a(1,1) (see Section 3.3) over 6-Myr interval (−6 to 0 Myr). Note that identifying $\bar{\Psi} + s_2$ in ϵ 's spectrum is obscured due to several large s_2 side peaks (see Fig. 5) that are unresolved over a 6-Myr interval.

^b $g_{43} = (g_4 - g_3)$. Note g - s interaction (see Zeebe, 2022).

that the dominant g_i are positive and the dominant s_i are negative. For retrograde axial precession and retrograde nodal precession, the frequencies combine to a lower frequency. Thus, precession and obliquity frequencies are higher and lower than the luni-solar precession rate, respectively (inversely for the periods, see Table 6 and Figs. 15 and 19).

Different approaches may be used to compute PT solutions. Some methods are based on series expansions or integration of equations for the angles involved (e.g., Sharaf and Boudnikova, 1967; Berger, 1976; Kinoshita, 1975, 1977; Berger et al., 1989; Laskar et al., 1993). Other methods are based on integrating equations for Earth's spin vector (e.g., Goldreich, 1966; Quinn et al., 1991; Touma and Wisdom, 1994; Zeebe, 2022). The latter approach allows physical insight into the torques involved (see Appendix A), provides a simple error metric for accuracy during spin vector integration, and can be applied using the most up-to-date orbital solutions (see Sections 2.5 and 3.4). Numerical routines to compute PT solutions based on Earth's spin vector are freely available in C (**snvec**) and R (**snvecR**) at github.com/rezeebe/snvec and github.com/japhir/snvecR.

As noted above, axial precession is retrograde, that is, the equinoxes move in the opposite direction to Earth's orbital motion and spin (see Fig. 14). Given the rule that angles measured in the orbital plane are increasing eastward (prograde or anticlockwise, see Fig. 2), it follows $\dot{\phi}_0 < 0$ (Zeebe and Lourens, 2022a; Zeebe, 2022). Note that the *general precession* (usually denoted as p_A , see below) is often used in this context with $\dot{p}_A > 0$ at t_0 (e.g., Lieske et al., 1977; Williams, 1994). For appropriate initial conditions that refer to the same reference epoch (e.g., $p_A(0) = \phi(0) = 0$), it follows $p_A = -\phi$ (see Section 3.2).

3.2. Luni-Solar (Equatorial) and Planetary (Ecliptic) Precession

As mentioned above (and pointed out before, e.g., Williams, 1994; Hilton et al., 2006), confusion may also arise over precession because of different notations and symbols. For

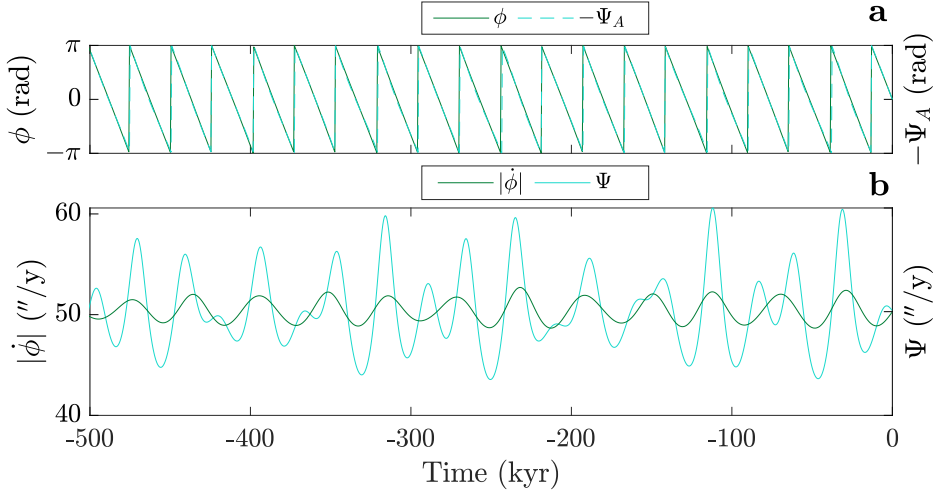


Figure 16: (a) Precession angle ϕ (in moving ecliptic frame, see Fig. 14) and $-\Psi_A$ (in inertial frame); both angles are taken as zero at t_0 . (b) Time derivative of precession angle $|\dot{\phi}|$ (in moving ecliptic frame) and luni-solar precession Ψ (in inertial frame). Ψ is conventionally taken positive. Note that Ψ is not constant over time and the difference $|\dot{\phi}| - \Psi$ (ecliptic motion) is small at t_0 , but not in general.

example, *luni-solar precession* and *planetary precession* (see below) may formally be referred to as *precession of the equator* and *precession of the ecliptic*, respectively (Fukushima, 2003; Hilton et al., 2006). The two quantities are critical for understanding the link between solar system dynamics and spin axis dynamics, and hence between OS and PT solutions.

The luni-solar precession rate (here symbol Ψ , see Table 1) at t_0 ($\Psi_0 > 0$) may be calculated from (e.g., Ward, 1974; Quinn et al., 1991; Williams, 1994):

$$\Psi_0 = \alpha \cos \epsilon_0 + \gamma_{gp} , \quad (9)$$

where α is often referred to as precession “constant” (Appendix A, although cf. Section 3.2.1), ϵ_0 is the obliquity angle at t_0 , and γ_{gp} is the geodetic precession (for details, see Quinn et al., 1991; Zeebe, 2022). Eq. (9) strictly only applies at t_0 and does not capture certain periodic variations (with long-term zero averages though). Note that Ψ is a rate (unit $''y^{-1}$), not an angle (the angle is usually denoted as Ψ_A , index ‘A’ for accumulated). Ψ refers to the total precessional space motion in an inertial coordinate system (fixed ecliptic, see Williams, 1994). However, for many applications, the motion relative to the moving ecliptic may be relevant (not to be confused with the moving equinoxes, see Section 3.1). As discussed in Section 2, the planetary orbits are not stationary but move in space over time due to mutual interactions. Thus, the motion of Earth’s orbital plane (ecliptic) contributes to the precessional motion (planetary or ecliptic precession, see Fig. 14, small blue arrow). The precession relative to the moving ecliptic is referred to as *general precession in longitude* ($p_A = -\phi$, see Fig. 14), or just *general precession*. Note that p_A is an angle; its rate is $dp_A/dt = \dot{p}_A$. In summary, with respect to ϕ , we may write:

$$\phi = -p_A \quad ; \quad \dot{\phi} = -\dot{p}_A . \quad (10)$$

Briefly, the important difference between ϕ and $\dot{\phi}$ vs. Ψ and $\dot{\Psi}$ is that the first two are measured in the moving ecliptic frame, while the last two are measured in the inertial frame.

Once \dot{p}_A and Ψ have been calculated, the precession components are often separated into a luni-solar and planetary contribution. At t_0 , the difference $\dot{p}_A - \Psi$ (*ecliptic motion*) may be written as (Williams, 1994):

$$\dot{p}_{A,0} - \Psi_0 = 50.2880 - 50.3848 = -0.0968 \quad ['' \text{ y}^{-1}] , \quad (11)$$

where Capitaine et al. (2003)'s values have been used (see Table 1). Similar values have been obtained based on a variety of approaches (e.g., Lieske et al., 1977; Laskar et al., 1993; Williams, 1994; Simon et al., 1994; Roosbeek and Dehant, 1998; Capitaine et al., 2003; Fukushima, 2003; Hilton et al., 2006; Vondrák et al., 2011). From Eq. (11) it may appear that the ecliptic motion is much smaller than the general motion. However, Eq. (11) only applies to the ecliptic vs. general motion at t_0 and not generally at all times (see Fig. 16 and Vondrák et al. (2011)).

For certain paleo-applications such as deep-time studies, the details and differences between the various precessional quantities discussed above may not matter because the long-term means of, e.g., Ψ , $|\dot{\phi}|$, and Eq. (9) are very similar. However, it is clear that Ψ , for instance, is not constant over time but varies periodically on Milanković time scales and exhibits long-term secular trends (Figs. 16 and 19). Moreover, its precise value depends on the precessional model employed and the dynamical ellipticity value at t_0 (see Section 3.3). Thus, providing precessional parameters or Ψ_0 with a large number of digits appears unnecessary for practical applications (except for check values in numerical routines).

3.2.1. Luni-Solar Precession: Long-term Variations

Considering only short-term variations in Ψ (see Eq. (9)), the parameter α may be indeed be taken as constant (see Appendix A). However, considering long-term variations in Ψ , α is far from constant due to the long-term evolution of the Earth-Moon system, including changes in Earth's rotation, lunar distance, tidal dissipation, dynamical ellipticity, etc. (see Section 3.5). For instance, ignoring the small term γ_{gp} and setting $\kappa = g_L = 1$ (see Appendix A), Eq. (9) may be re-written as:

$$\Psi = \mathcal{C} \frac{H}{\Omega_E} \left(1 + \frac{a^3}{a_L^3} \frac{m_L}{M_S} \right) \cos \epsilon , \quad (12)$$

where $\mathcal{C} = \frac{3}{2} \frac{GM}{a^3}$, H is the dynamical ellipticity (see Section 3.3), Ω_E is Earth's angular speed, a the semi-major axis of its orbit, a_L the Earth-Moon distance parameter, and m_L/M_S the lunar to solar mass ratio. Furthermore, $H \propto \Omega_E^2$ (see Section 3.3) and hence:

$$\Psi = \mathcal{D} \Omega_E \left(1 + \frac{a^3}{a_L^3} \frac{m_L}{M_S} \right) \cos \epsilon , \quad (13)$$

where \mathcal{D} may be taken as constant (to first order) over long time scales. Eq. (13) illustrates the large secular decrease in Ψ over geologic time (i.e, increase in period, see Fig. 19) due to the slow-down of Earth's rotation (Ω_E) and the simultaneous increase in lunar distance (a_L). The two processes are coupled via conservation of angular momentum (e.g., Goldreich, 1966; Touma and Wisdom, 1994; Farhat et al., 2022; Zeebe and Lantink, 2024b; Malinverno and

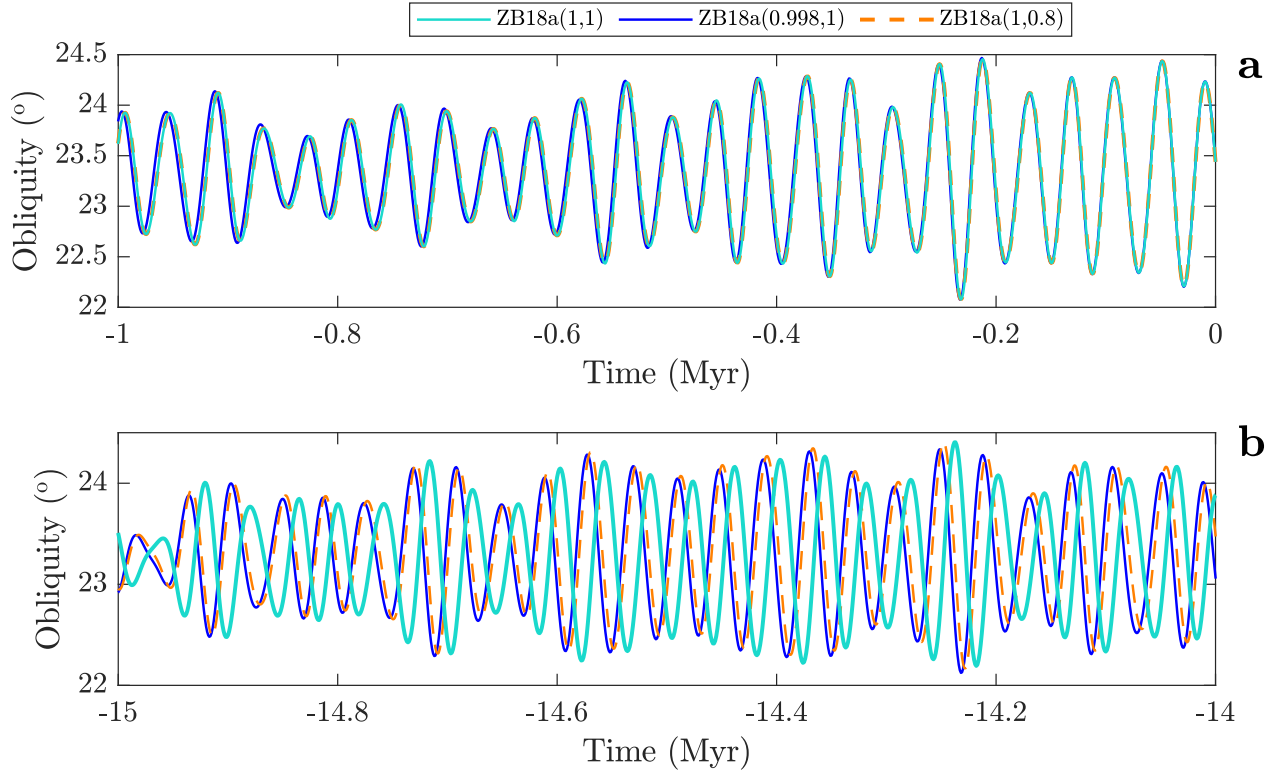


Figure 17: Illustration of changes in Earth’s dynamical ellipticity (E_d) and tidal dissipation (T_d) affecting the numerical solution for Earth’s obliquity over 15 Myr (for details on the numerical parameters E_d and T_d , see Zeebe and Lourens, 2022a). In runs labeled $E_d = 0.998$ and $T_d = 0.8$, the values of E_d and T_d were set to 99.8% and 80%, respectively, of their modern values $E_d = T_d = 1.0$. (a) -1 to 0 Myr, the solutions are nearly identical. (b) -14 to -15 Myr, the solutions are out of phase, which would cause significant dating errors.

Meyers, 2024). Finally, note that several recent studies have estimated long-term variations in luni-solar precession frequency from stratigraphic data (see, e.g., Wu et al., 2024, and references therein).

3.3. Dynamical Ellipticity and Tidal Dissipation

Dynamical ellipticity refers to the gravitational shape of the Earth, largely controlled by the hydrostatic response to its rotation rate. Dynamical ellipticity is defined as $H = [C - (A + B)/2]/C$, where C is the polar moment of inertia and A and B are the equatorial moments of inertia. If $A = B$,

$$H = (C - A)/C \quad ; \quad H \propto \Omega_E^2 . \quad (14)$$

Importantly, H ’s hydrostatic response is proportional to Ω_E^2 , where Ω_E is Earth’s spin, or angular velocity (Lambeck, 1980). The present value of H is ~ 0.00328 ; however, its precise, absolute value is usually adjusted to other parameters and hence may differ between models (e.g., Quinn et al., 1991; Laskar et al., 1993; Williams, 1994; Capitaine et al., 2003; Chen et al., 2015; Zeebe, 2022). Note that the calculated changes in obliquity and precession in the past are sensitive to even small changes in dynamical ellipticity (see Fig. 17), which is affected by, e.g., Ω_E , ice volume, and mantle convection (e.g., Berger et al., 1989; Laskar

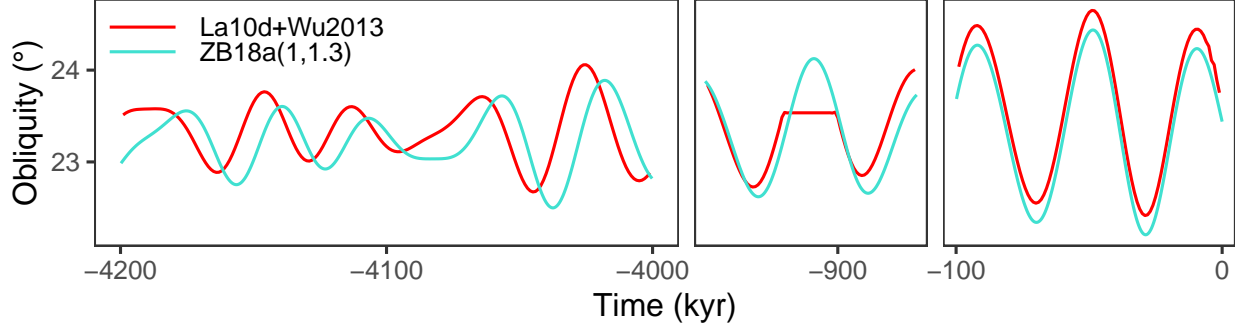


Figure 18: Obliquity solution based on the procedure by Wu et al. (2013) for La10x currently available in the `Acycle` package (Li et al., 2019) (example: La10d+Wu2013, red). For comparison, obliquity calculated using `snvec` (Zeebe and Lourens, 2022b) based on ZB18a (Zeebe and Lourens, 2019) (ZB18a(1,1.3), turquoise, see text for details).

et al., 1993; Morrow et al., 2012; Zeebe and Lourens, 2022a). Regarding the effect of Earth’s dynamical ellipticity and Earth’s rotation rate on the luni-solar precession rate (see Eq. (9)), it is important that the precession constant α is proportional to H and inversely proportional to Ω_E (see Appendix A). Thus, because $H \propto \Omega_E^2$,

$$\alpha \propto \Omega_E . \quad (15)$$

Tidal dissipation refers to the energy dissipation in the earth and ocean, which reduces Earth’s rotation rate and increases the length of day and the Earth-Moon distance. The parameter relevant here for PT solutions is the change in lunar mean motion n_L (average angular frequency), which is presently decreasing at a rate:

$$Q_0 = (dn_L/dt)_0/(n_L)_0 = -4.6 \times 10^{-18} \text{ s}^{-1} \quad (16)$$

(Quinn et al., 1991). Reconstructing T_d ’s history involves considerable uncertainties and remains an active area of research, specifically the development of model frameworks for the Earth-Moon’s tidal evolution focusing on the long-term history of ocean tidal dissipation (e.g., Webb, 1982; Hansen, 1982; Kagan and Maslova, 1994; Green et al., 2017; Motoyama et al., 2020; Daher et al., 2021; Tyler, 2021; Farhat et al., 2022; Zeebe and Lantink, 2024b).

The combined precession-tilt-orbital solution may be denoted as $\text{OS}(E_d, T_d)$, see Zeebe and Lourens (2022a). For example, ZB18a(1,1) refers to a PT solution based on the orbital solution ZB18a with modern values $E_d = 1$ and $T_d = 1$ (see Figs. 15 and 17). Relatively simple parameterizations using E_d and T_d as employed in Zeebe and Lourens (2022a) are most useful over, say, the Cenozoic, where changes in Ψ , Earth-Moon distance, etc. are comparatively small (Quinn et al., 1991; Zeebe and Lourens, 2022a; Zeebe, 2022). In order to compute full PT solutions in deep time, say, on Gyr-time scale, a fundamentally different approach is required that considers the long-term evolution of the Earth-Moon system, as well as the large scale dynamical chaos in the solar system (see Sections 3.2.1, 3.5 and Zeebe and Lantink, 2024a,b).

3.4. Up-to-date Precession and Obliquity Solutions

Wu et al. (2013) suggested and employed a procedure to obtain obliquity and precession solutions using the orbital solutions La10x from Laskar et al. (2011) and the Fortran code

from Laskar et al. (1993) (for an example following Wu et al. available in the `Acycle` package (Li et al., 2019), see Fig. 18). Wu et al. (2013) used the parameter values $\text{FGAM} = 1.0$ and $\text{CMAR} = 1.3$. Importantly, the Wu et al. (2013) procedure/output has also been used in subsequent studies (e.g., Laurin et al., 2015; Ma et al., 2017, 2019). However, the `La10x` output is incompatible with the 1993-Fortran routine because of different reference frames (see below). Here we illustrate the problematic obliquity solution by comparison with Zeebe and Lourens (2019), from which we calculate obliquity using `snvec` (Zeebe and Lourens, 2022b) and the values for $E_d = 1$ and $T_d = 1.3$. The `Acycle` output is offset already at $t = 0$ (see Fig. 18). Furthermore, at around -900 kyr, part of the cycle is clipped, which appears to be a numerical error. At around -4 Myr the Wu et al. (2013) solution is offset from Zeebe and Lourens (2022b) by about half a cycle.

The problem with the approach of Wu et al. (2013) is incompatible reference frames (see Section 2.1.2). The 1993-Fortran routines from Laskar et al. (1993) expect orbital elements given in the ecliptic reference frame. However, the `La10x` elements are given in the invariant reference frame (Laskar et al., 2011). As explained above, the invariant frame is based on the invariable plane (perpendicular to the solar system’s total angular momentum vector that passes through its barycentre) and is hence different from the ecliptic frame. Wu et al.’s procedure is therefore not recommended. For the user interested in PT solutions based on up-to-date orbital solutions, say, for the Cenozoic, the freely available routines `snvec` and `snvecR` are recommended (github.com/rezeebe/snvec and github.com/japhir/snvecR). These routines can be used with up-to-date orbital solutions such as ZB18a and ZB20x that supply orbital elements in a compatible reference frame. For the application-oriented user, pre-computed and up-to-date PT solutions for different E_d and T_d values are readily available for download (no programs, coding, etc. involved), see www.ncdc.noaa.gov/paleo/study/35174 (Zeebe and Lourens, 2022a). PT solutions here refer to full solutions (including individual PT cycles and temporal resolution of order 10^2 - 10^3 y), rather than calculated frequencies and long-term averages.

3.5. Milanković Forcing in Deep Time

This review has largely focused on the past few 100 Myr. Milanković forcing for older intervals (deep time) needs to consider a host of additional factors, including tidal dissipation, the long-term evolution of the Earth-Moon system, solar mass loss, and more. Unfortunately, a comprehensive review of astronomical forcing in deep time is beyond the scope of this paper. Instead, we refer the reader to recent work specifically dedicated to Milanković forcing in deep time (Zeebe and Lantink, 2024a,b), as well as related studies (e.g., MacDonald, 1964; Goldreich, 1966; Mignard, 1981; Berger et al., 1989; Ito et al., 1993; Touma and Wisdom, 1994; Ito et al., 1995; Waltham, 2015; Meyers and Malinverno, 2018; Spalding et al., 2018; Farhat et al., 2022; De Vleeschouwer et al., 2024; Malinverno and Meyers, 2024). The evolution of the main periods of eccentricity, tilt, and precession (ETP) on Gyr-time scale may be summarized in a nutshell as follows (see Fig. 19). The average precession and obliquity periods ($\bar{\Psi} + g_i$ and $\bar{\Psi} + s_i$) increase with time due to the changing luni-solar precession $\bar{\Psi}$ (averaged over 20 Myr intervals), accompanied by the slowing of Earth’s rotation, lengthening of the day, and the receding Moon. The short eccentricity periods ($\sim 95, 99, 124$, and 131 kyr recent) appear relatively stable but actually exhibit substantial variations in frequency and amplitude and

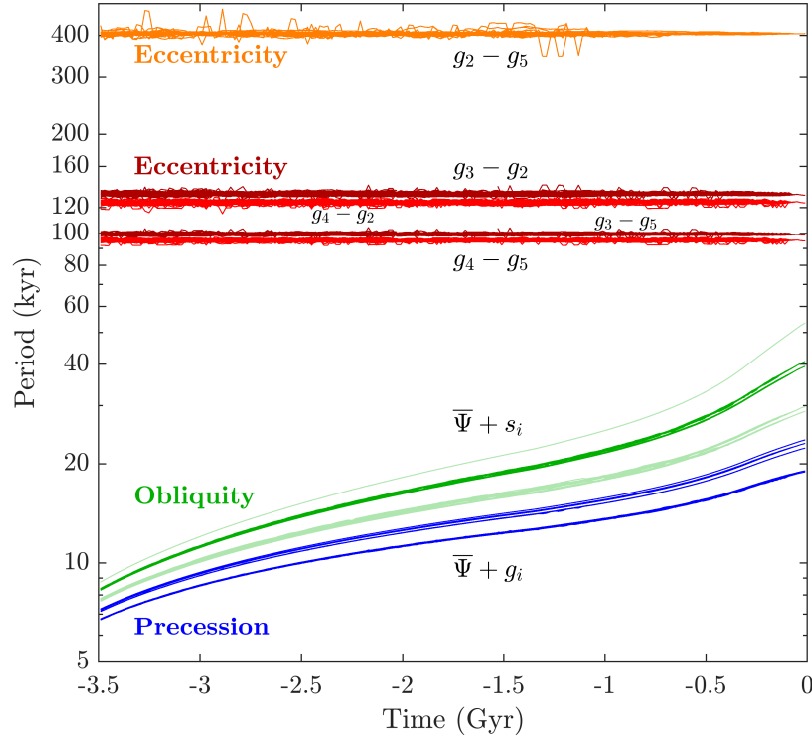


Figure 19: Summary of eccentricity, tilt, and precession (ETP) periods from 3.5-Gyr integrations (Zeebe and Lantink, 2024a,b). Note the logarithmic ordinate. $\bar{\Psi}$ refers to the averaged luni-solar precession over 20 Myr intervals.

do not serve as metronomes (Zeebe and Lantink, 2024b). The spikes in the long eccentricity cycle ($g_2 - g_5$) (top, Fig. 19) reflect instabilities in g_2 , which compromises the 405-kyr cycle’s reliability beyond several hundred million years in the past, as mentioned above (Zeebe and Lantink, 2024a). One major issue identified by Zeebe and Lantink (2024a) is that the long eccentricity cycle may not be available as a primary tuning target in deep time.

Importantly, the direct use of astronomical solutions for astronomical tuning (e.g., for absolute ages and chronologies across the Cenozoic) represents only one realm of the use of astronomical solutions in astrochronology. As pointed out in Section 1, much of the ongoing astrochronological work on the geologic time scale uses relative (floating) age models, spanning most of Earth’s history, that is, the entire pre-Cenozoic. Pre-Cenozoic studies also rely on astronomical solutions in a range of capacities, even when explicit cycle-to-cycle tuning in the time domain is not possible due to uncertainties in amplitude, phase, and frequency of the forcing due to chaos and uncertainties in parameters such as tidal dissipation, dynamical ellipticity, etc. For more information on pre-Cenozoic astronomical parameters, we refer the reader to recent theoretical work (e.g., Spalding et al., 2018; Daher et al., 2021; Tyler, 2021; Farhat et al., 2022; Zeebe and Lantink, 2024a,b), as well as observational work using the geologic record (e.g., Zhang et al., 2015; Ma et al., 2017; Meyers and Malinverno, 2018; Kent et al., 2018; Lantink et al., 2019; Olsen et al., 2019; Sørensen et al., 2020; Lantink et al., 2022, 2023, 2024; Malinverno and Meyers, 2024; Wu et al., 2024).

This section concludes our review of orbital solutions and precession-tilt solutions. The remaining sections deal with practical considerations, summary, and outlook.

4. Practical Considerations

In the following, we provide a few recommendations and list selected resources for practical consideration. First, regarding orbital solutions, the user needs to consider their valid time span, which is limited fundamentally by solar system chaos (see Table 5). As pointed out above, the probability that a particular OS represents the actual, unique history of the solar system is near zero significantly beyond the OS’s validity range. For example, finding a good match between, say an eccentricity record at 100 Ma and La04 would be entirely coincidental and concluding that La04 is therefore a proper solution of the solar system orbits over the past 100 Myr would be misleading (see Section 2.5). Instead, for the time being, we recommend the solutions ZB18a and ZB20x across the time span from -300 to 0 Myr, available at www.ncdc.noaa.gov/paleo/study/36415 and www2.hawaii.edu/~zeebe/Astro.html. Note though that these solutions have been constrained by geologic data only up to an age of 66 Ma (Table 5). Beyond -300 Myr, the ZB23x solutions may serve as possible templates for deep time characteristics (see www.ncdc.noaa.gov/paleo/study/39199). Importantly, however, no single solution should be considered the “true” solution.

For up-to-date precession-tilt solutions, we recommend choosing between two options at this time (see Section 3.4). One option is downloading pre-calculated PT solutions for different values of E_d and T_d , available at www.ncdc.noaa.gov/paleo/study/35174 and www2.hawaii.edu/~zeebe/Astro.html (see Zeebe and Lourens, 2022a; Zeebe, 2022). Another option is for the user to generate their own PT solutions based on up-to-date orbital solutions using our `snvec` code in C or R available at github.com/rezeebe/snvec and github.com/japhir/snvecR (for summary, see Table 7). We do not recommend the procedure proposed by Wu et al. (2013) to generate PT solutions (see Section 3.4). For the user interested in generating insolation curves based on up-to-date orbital solutions, we mention here a web-based user interface currently under construction at astrocyclo.soest.hawaii.edu.

4.1. Available Resources

To assist the user in identifying available resources for the analysis of their specific problem at hand, we list a few selected solutions, codes, and tools (including URLs, see Table 7). The list is far from exhaustive and focuses on resources that are up-to-date (including OS/PT solutions), open source, directly accessible, frequently used, and maintained. Assume the user’s goal is, for example, to develop a cyclostratigraphic age model for a Miocene record based on astronomical tuning to Earth’s precession and obliquity. For the time series analysis of the data record, tools such as `astrochron` and `Acycle` are available (Table 7). For the astronomical tuning to precession and obliquity, PT solutions based on ZB18a with different values for E_d and T_d are available for download at www2.hawaii.edu/~zeebe/Astro.html (Zeebe and Lourens, 2022a; Zeebe, 2022). Given a task/time interval at hand and the information compiled in Tables 5 and 7, most users seeking guidance should be able to identify resources for the analysis of their problem using astronomical solutions and Milanković forcing as reviewed in the present paper. The experienced user is of course free to employ the tools of their choice. However, regarding astronomical solutions, we strongly recommend considering the recency, limitations, and valid time span of the solutions (see Sections 2.5 and 3.4). Tools that yield inaccurate results should be abandoned (see Section 3.4).

Table 7: Selected resources (up-to-date OS/PT solutions, open source, directly accessible, frequently used, maintained).

Resource Type	Name/ID	Reference	URL
Orbital Solution	ZB23x	Zeebe and Lantink (2024a)	<i>a,b</i>
Orbital Solution	ZB18a ZB20x	Zeebe and Lourens (2019, 2022b)	<i>c,a</i>
Orbital Solution	La10x	Laskar et al. (2011)	<i>d</i>
PT Solution	ZB18a(E_d, T_d)	Zeebe and Lourens (2022a) ; Zeebe (2022)	<i>e,a</i>
Insolation web-interface	astrocyclo	under construction	<i>f</i>
Orbit Integrator+Code (C)	orbitN	Zeebe (2023)	<i>g,a</i>
PT Integrator+Code (C, R)	snvec snvecR	Zeebe (2022)	<i>h,a</i>
Integrator+Code (C, Python)	rebound	Rein and Liu (2012)	<i>i</i>
Astrochronology Tool (R)	astrochron	Meyers (2014)	<i>j</i>
Time Series Analysis Tool	Acycle	Li et al. (2019)	<i>k</i>

^a www2.hawaii.edu/~zeebe/Astro.html

^b www.ncdc.noaa.gov/paleo/study/39199

^c www.ncdc.noaa.gov/paleo/study/26970 | www.ncdc.noaa.gov/paleo/study/36415

^d vo.imcce.fr/insola/earth/online/earth/La2010/index.html

^e www.ncdc.noaa.gov/paleo/study/35174

^f astrocyclo.soest.hawaii.edu

^g github.com/rezeebe/orbitN

^h github.com/rezeebe/snvec | github.com/japhir/snvecR

ⁱ rebound.readthedocs.io/en/latest

^j cran.r-project.org/web/packages/astrochron/index.html

^k acycle.org

5. Summary & Outlook

We have reviewed astronomical solutions and Milanković forcing as applied in the Earth sciences. Given confusion and recent inaccurate results in the application of astronomical solutions, our review appears appropriate and timely, and clarifies the astronomical basis, applicability, and limitations of astronomical solutions. Applying accurate and up-to-date solutions and tools is critical to extend and improve the astronomical time scale, which, over the past few decades, has transformed the dating of geologic archives. Today, astronomical solutions and the astronomical time scale represent the backbone of astrochronology and cyclostratigraphy, widely used in the Earth sciences. In our review, we have discussed two fundamental types of astronomical solutions and their limitations: orbital solutions (OSs) and precession-tilt (PT) solutions. While OSs are a prerequisite and essential for PT solutions, the reverse effects of rotational dynamics on OSs are generally minor.

To understand the behavior of orbital solutions and astronomical forcing terms, we have emphasized the analysis of the fundamental (secular) frequencies, which may be thought of as the spectral building blocks of the dynamical system. The secular frequency analysis also provides insight into amplitude and frequency modulation of orbital forcing signals

and leads to the conclusion that the current evidence does not support the notion of generally stable and prominent astronomical “metronomes” for universal use in astrochronology and cyclostratigraphy. Large-scale dynamical chaos is an inherent characteristic of the solar system and fundamental to understanding the behavior of astronomical solutions and their limitations. We have illustrated the unpredictability and unaccountability of chaotic systems in terms of basic statistics. One important corollary is that it is generally not possible to “tune” or “fit” astronomical solutions to geological data. The best that can probably be done is to create large ensembles of solutions via parameter variations and select/discard those solutions that show good/poor agreement with the data. Our in-depth description of the various quantities associated with Earth’s axial precession should aid in clarifying the terminology and notation appearing in the literature. We have also discussed astronomical forcing and astrochronology in deep time, which represents another critical application of astronomical solutions beyond the direct use for astronomical tuning of, say, absolute Cenozoic ages and chronologies. Finally, our summary of selected available resources should assist the interested user in identifying resources for the analysis of their specific problem at hand, using the astronomical solutions and Milanković forcing as reviewed here.

Continuing improvements in computer technology, speed, and algorithms will accelerate numerical computations in the future and will allow integrating more complete and complex models of the solar system (for recent endeavors, see, e.g., [Brown and Rein, 2020](#); [Zeebe, 2023](#); [Javaheri et al., 2023](#); [Hernandez and Dehnen, 2024](#)). Importantly, however, the limits imposed by dynamical chaos on astronomical calculations and geological/astrochronological applications are fundamental and physical in nature, and cannot be overcome by numerical advances. In order to generate ensemble solutions with long (and specific) divergence times, arbitrary precision code might be helpful. One goal regarding user access to up-to-date astronomical solutions in the future is offering more user-friendly applications, such as a web-based user interface (for current efforts in progress/under construction, see, e.g., [astrocyclo.soest.hawaii.edu](#)). In terms of future observational endeavors, it is highly desirable to obtain high-quality cyclostratigraphic sequences that constrain the evolution of Earth’s precession and obliquity frequencies across the Cenozoic, as well as in deep time, the latter being critical to reconstructing the Earth-Moon system’s long-term evolution. (see, e.g., [Wu et al., 2024](#), and references therein). New high-quality eccentricity and obliquity records older than ~50 Ma will be crucial in constraining the solar system’s chaotic history, and in turn, in providing highly accurate geological dates and chronologies for cyclostratigraphy and astrochronology.

Acknowledgments. We thank one anonymous reviewer, Dorian Abbot, Alberto Malinverno, and Steve Meyers for their thorough reviews, which improved the paper. We are grateful to Alberto Malinverno and Steve Meyers for specific text suggestions that refined and extended the manuscript content. We also thank David M. Hernandez and Margriet Lantink for helpful comments on the manuscript draft. This research was supported by Heising-Simons Foundation Grant #2021-2800 and U.S. NSF grant OCE20-34660 to R.E.Z.

software `orbitN`, [github.com/rezeebe/orbitN](#), `snvec`, [github.com/rezeebe/snvec](#), `snvecR`, [github.com/japhir/snvecR](#)

Appendix A. Precession Equations

The calculation of precession and obliquity using our `snvec` code is detailed in Zeebe (2022) and Zeebe and Lantink (2024b). A few equations for the precession constant are included here for clarity (see Section 3). The change in the spin axis (unit vector \mathbf{s}) is calculated from (e.g., Goldreich, 1966; Ward, 1974, 1979; Bills, 1990; Quinn et al., 1991):

$$\dot{\mathbf{s}} = \alpha(\mathbf{n} \cdot \mathbf{n})(\mathbf{s} \times \mathbf{n}) , \quad (\text{A.1})$$

where α is the precession constant (although cf. Section 3.2.1) and \mathbf{n} the orbit normal (unit vector normal to the orbit plane). The obliquity (polar) angle, ϵ , is given by:

$$\cos \epsilon = \mathbf{n} \cdot \mathbf{s} . \quad (\text{A.2})$$

The precession (azimuthal) angle, ϕ , measures the motion of \mathbf{s} in the orbit plane. The precession constant α is calculated from (e.g., Quinn et al., 1991):

$$\alpha = K (\kappa + \beta) , \quad (\text{A.3})$$

where $\kappa = (1 - e^2)^{-3/2}$ and e is the orbital eccentricity. K and β relate to the torque due to the Sun and Moon, respectively:

$$K = \frac{3}{2} \frac{C - A}{C} \frac{1}{\Omega_E a^3} GM_S \quad (\text{A.4})$$

$$\beta = g_L \frac{a^3}{a_L^3} \frac{m_L}{M_S} , \quad (\text{A.5})$$

where A and C are the planet’s equatorial and polar moments of inertia, $(C - A)/C = H$ is the dynamical ellipticity, Ω_E is Earth’s angular speed, a the semi-major axis of its orbit, a_L is the Earth-Moon distance parameter, and GM is the gravitational parameter of the Sun (see Table 1). The index ‘ L ’ refers to lunar properties, where g_L is a correction factor related to the lunar orbit (Kinoshita, 1975, 1977; Quinn et al., 1991) and m_L/M_S is the lunar to solar mass ratio. The parameter values used for Earth are given in Table 1 and in Zeebe (2022). With K and β , α and hence the luni-solar precession rate Ψ can be calculated (see Eq. (9)).

References

- Abbot, D.S., Hernandez, D.M., Hadden, S., Webber, R.J., Afentakis, G.P., Weare, J., 2023. Simple Physics and Integrators Accurately Reproduce Mercury Instability Statistics. *Astrophys. J.* 944, 190. doi:[10.3847/1538-4357/acb6ff](https://doi.org/10.3847/1538-4357/acb6ff), [arXiv:2212.14844](https://arxiv.org/abs/2212.14844).
- Antoñana, M., Alberdi, E., Makazaga, J., Murua, A., 2022. An implicit symplectic solver for high-precision long-term integrations of the Solar System. *Celest. Mech. Dynamic. Astron.* 134, 31. doi:[10.1007/s10569-022-10081-9](https://doi.org/10.1007/s10569-022-10081-9).
- Applegate, J.H., Douglas, M.R., Gürsel, Y., Hunter, P., Seitz, C.L., Sussman, G.J., 1985. A Digital Orrery. *IEEE Trans. Comput.* 34, 822–831. doi:[10.1109/TC.1985.1676638](https://doi.org/10.1109/TC.1985.1676638).
- Arnol’d, V.I., 1963. Proof of a Theorem of A. N. KOLMOGOROV on the Invariance of Quasi-Periodic Motions Under Small Perturbations of the Hamiltonian. *Russ. Math. Surv.* 18, 9–36. doi:[10.1070/RM1963v018n05ABEH004130](https://doi.org/10.1070/RM1963v018n05ABEH004130).
- Aubry, M., Van Couvering, J., Christie-Blick, N., Landing, E., Pratt, B., Owen, D., Ferrusquía-Villafranca, I., 2009. Terminology of geological time: Establishment of a community standard. *Stratigraphy* 6, 100–105.
- Bate, R.R., Mueller, D.D., White, J.E., 1971. *Fundamentals of Astrodynamics*. Dover, New York.
- Batygin, K., Laughlin, G., 2008. On the dynamical stability of the solar system. *Astrophys. J.* 683, 1207–1216. doi:[10.1086/589232](https://doi.org/10.1086/589232).

- Berger, A., 1977. Long-Term Variations of the Earth's Orbital Elements. *Celestial Mechanics* 15, 53–74. doi:[10.1007/BF01229048](https://doi.org/10.1007/BF01229048).
- Berger, A., 1978. Long-term variations of daily insolation and Quaternary climatic changes. *J. Atmos. Sci.* 35, 2362–2367.
- Berger, A., Loutre, M.F., 1992. Astronomical solutions for paleoclimate studies over the last 3 million years. *Earth Planet. Sci. Lett.* 111, 369–382. doi:[10.1016/0012-821X\(92\)90190-7](https://doi.org/10.1016/0012-821X(92)90190-7).
- Berger, A., Loutre, M.F., 1994. Precession, eccentricity, obliquity, insolation and paleoclimates, in: J.-C. Duplessy and M.-T. Spyridakis (Ed.), *Long-term Climatic Variations*, Springer Berlin Heidelberg. pp. 107–151. doi:[10.1007/978-3-642-79066-9_5](https://doi.org/10.1007/978-3-642-79066-9_5).
- Berger, A., Loutre, M.F., Dehant, V., 1989. Influence of the changing lunar orbit on the astronomical frequencies of pre-Quaternary insolation patterns. *Paleoceanogr.* 4, 555–564. doi:[10.1029/PA004i005p00555](https://doi.org/10.1029/PA004i005p00555).
- Berger, A.L., 1976. Obliquity and precession for the last 5000000 years. *Astron. Astrophys.* 51, 127–135.
- Bills, B.G., 1990. The rigid body obliquity history of Mars. *J. Geophys. Res.* 95, 14137–14153. doi:[10.1029/JB095iB09p14137](https://doi.org/10.1029/JB095iB09p14137).
- Bretagnon, P., 1974. Long-period terms in the solar system. (in French) *Astron. Astrophys.* 30, 141–154.
- Broecker, W.S., 1966. Absolute Dating and the Astronomical Theory of Glaciation: Changes in climate occur in response to periodic variations in the earth's tilt and precession. *Science* 151, 299–304.
- Broecker, W.S., 1985. *How to Build a Habitable Planet*. pp. 291. Eldigio Press, Lamont-Doherty Geological Observatory, Palisades, New York.
- Brouwer, D., van Woerkom, A.J.J., 1950. The secular variations of the orbital elements of the principal planets. *Astronomical Papers Prepared for the Use of the American Ephemeris and Nautical Almanac* 13, 81–107.
- Brown, G., Rein, H., 2020. A Repository of Vanilla Long-term Integrations of the Solar System. *Res. Notes American Astron. Soc.* 4, 221. doi:[10.3847/2515-5172/abd103](https://doi.org/10.3847/2515-5172/abd103), [arXiv:2012.05177](https://arxiv.org/abs/2012.05177).
- Capitaine, N., Wallace, P.T., Chapront, J., 2003. Expressions for IAU 2000 precession quantities. *Astron. Astrophys.* 412, 567–586. doi:[10.1051/0004-6361:20031539](https://doi.org/10.1051/0004-6361:20031539).
- Charbonnier, G., Boulila, S., Spangenberg, J.E., Vermeulen, J., Galbrun, B., 2023. Astrochronology of the Aptian stage and evidence for the chaotic orbital motion of Mercury. *Earth Planet. Sci. Lett.* 610, 118104. doi:[10.1016/j.epsl.2023.118104](https://doi.org/10.1016/j.epsl.2023.118104).
- Chen, W., Li, J.C., Ray, J., Shen, W.B., Huang, C.L., 2015. Consistent estimates of the dynamic figure parameters of the earth. *J. Geodesy* 89, 179–188. doi:[10.1007/s00190-014-0768-y](https://doi.org/10.1007/s00190-014-0768-y).
- Chirikov, B.V., 1979. A universal instability of many-dimensional oscillator systems. *Phys. Rep. (Rev. Sec. Phys. Lett.)* 52, 263–379. doi:[10.1016/0370-1573\(79\)90023-1](https://doi.org/10.1016/0370-1573(79)90023-1).
- Cvijanovic, I., Lukovic, J., Begg, J.D., 2020. One hundred years of Milanković cycles. *Nat. Geosci.* 13, 524–525. doi:[10.1038/s41561-020-0621-2](https://doi.org/10.1038/s41561-020-0621-2).
- Daher, H., Arbic, B.K., Williams, J.G., Ansong, J.K., Boggs, D.H., Müller, M., Schindelegger, M., Austermann, J., Cornuelle, B.D., Crawford, E.B., Fringer, O.B., Lau, H.C.P., Lock, S.J., Maloof, A.C., Menemenlis, D., Mitrovica, J.X., Green, J.A.M., Huber, M., 2021. Long-Term Earth-Moon Evolution With High-Level Orbit and Ocean Tide Models. *J. Geophys. Res. (Planets)* 126, e06875. doi:[10.1029/2021JE006875](https://doi.org/10.1029/2021JE006875).
- Danby, J.M.A., 1988. *Fundamentals of celestial mechanics*. Willmann-Bell Inc., Richmond, VA.
- De Vleeschouwer, D., Percival, L.M., Wichern, N.M., Batenburg, S.J., 2024. Pre-Cenozoic cyclostratigraphy and palaeoclimate responses to astronomical forcing. *Nature Rev. Earth Env.* 5, 59–74.
- Duriez, L., 1977. *Théorie Générale Planétaire en Variables Elliptiques. I. Développement des Équation*. (in French) *Astron. Astrophys.* 54, 93–112.
- Dutkiewicz, A., Boulila, S., Müller, R.D., 2024. Deep-sea hiatus record levels orbital pacing by 2.4 Ma eccentricity grand cycles. *Nature Comm.* 15. doi:[10.1038/s41467-024-46171-5](https://doi.org/10.1038/s41467-024-46171-5).
- Einstein, A., 1916. Die Grundlage der allgemeinen Relativitätstheorie. *Annalen der Physik*, VI. Folge 49(7), 769–822. doi:[10.1002/andp.19163540702](https://doi.org/10.1002/andp.19163540702).
- Emiliani, C., 1955. Pleistocene temperatures. *J. Geol.* 63, 538–578.
- Emiliani, C., 1995. Two revolutions in the Earth Sciences. *Terra Nova* 7, 587–597. doi:[10.1111/j.1365-3121.1995.tb00706.x](https://doi.org/10.1111/j.1365-3121.1995.tb00706.x).
- Farhat, M., Auclair-Desrotour, P., Boué, G., Laskar, J., 2022. The resonant tidal evolution of the Earth-Moon distance. *Astron. Astrophys.* 665, L1. doi:[10.1051/0004-6361/202243445](https://doi.org/10.1051/0004-6361/202243445), [arXiv:2207.00438](https://arxiv.org/abs/2207.00438).

- Fränz, M., Harper, D., 2002. Heliospheric coordinate systems. *Planet. Space Sci.* 50, 217–233. doi:[10.1016/S0032-0633\(01\)00119-2](https://doi.org/10.1016/S0032-0633(01)00119-2).
- Fukushima, T., 2003. A New Precession Formula. *Astron. J.* 126, 494–534. doi:[10.1086/375641](https://doi.org/10.1086/375641).
- Goldreich, P., 1966. History of the lunar orbit. *Rev. Geophys. Space Phys.* 4, 411–439. doi:[10.1029/RG004i004p00411](https://doi.org/10.1029/RG004i004p00411).
- Green, J.A.M., Huber, M., Waltham, D., Buzan, J., Wells, M., 2017. Explicitly modelled deep-time tidal dissipation and its implication for Lunar history. *Earth Planet. Sci. Lett.* 461, 46–53. doi:[10.1016/j.epsl.2016.12.038](https://doi.org/10.1016/j.epsl.2016.12.038).
- Hansen, K.S., 1982. Secular effects of oceanic tidal dissipation of the moon’s orbit and the earth’s rotation. *Rev. Geophys. Space Phys.* 20, 457–480. doi:[10.1029/RG020i003p00457](https://doi.org/10.1029/RG020i003p00457).
- Hays, J.D., Imbrie, J., Shackleton, N.J., 1976. Variations in the Earth’s Orbit: Pacemaker of the Ice Ages. *Science* 194, 1121–1132. doi:[10.1126/science.194.4270.1121](https://doi.org/10.1126/science.194.4270.1121).
- Herbert, T.D., 1992. Paleomagnetic calibration of Milankovitch cyclicity in Lower Cretaceous sediments. *Earth and Planet. Sci. Lett.* 112, 15–28. doi:[10.1016/0012-821X\(92\)90003-E](https://doi.org/10.1016/0012-821X(92)90003-E).
- Hernandez, D.M., Dehnen, W., 2024. Multiple time-step reversible N-body integrators for close encounters in planetary systems. *MNRAS* 530, 3870–3880. doi:[10.1093/mnras/stae985](https://doi.org/10.1093/mnras/stae985).
- Hernandez, D.M., Zeebe, R.E., Hadden, S., 2022. Stepsize errors in the N-body problem: discerning Mercury’s true possible long-term orbits. *MNRAS* 510, 4302–4307. doi:[10.1093/mnras/stab3664](https://doi.org/10.1093/mnras/stab3664), [arXiv:2111.08835](https://arxiv.org/abs/2111.08835).
- Hilgen, F., Zeeden, C., Laskar, J., 2020. Paleoclimate records reveal elusive 200-kyr eccentricity cycle for the first time. *Global Planet. Change* 194, 103296. doi:[10.1016/j.gloplacha.2020.103296](https://doi.org/10.1016/j.gloplacha.2020.103296).
- Hilgen, F.J., Abels, H.A., Kuiper, K.F., Lourens, L.J., Wolthers, M., 2015. Towards a stable astronomical time scale for the Paleocene: Aligning Shatsky Rise with the Zumaia–Walvis Ridge ODP Site 1262 composite. *Newsletters on Stratigraphy* 48, 91–110.
- Hilgen, F.J., Kuiper, K.F., Lourens, L.J., 2010. Evaluation of the astronomical time scale for the Paleocene and earliest Eocene. *Earth Planet. Sci. Lett.* 300, 139–151. doi:[10.1016/j.epsl.2010.09.044](https://doi.org/10.1016/j.epsl.2010.09.044).
- Hilton, J.L., Capitaine, N., Chapront, J., Ferrandiz, J.M., Fienga, A., Fukushima, T., Getino, J., Mathews, P., Simon, J.L., Soffel, M., Vondrak, J., Wallace, P., Williams, J., 2006. Report of the International Astronomical Union Division I Working Group on Precession and the Ecliptic. *Celest. Mech. Dynamic. Astron.* 94, 351–367. doi:[10.1007/s10569-006-0001-2](https://doi.org/10.1007/s10569-006-0001-2).
- Hinnov, L.A., 2000. New perspectives on orbitally forced stratigraphy. *Ann. Rev. Earth Planet. Sci.* 28, 419–475. doi:[10.1146/annurev.earth.28.1.419](https://doi.org/10.1146/annurev.earth.28.1.419).
- Hinnov, L.A., 2018. Cyclostratigraphy and Astrochronology in 2018, in: Montenari, M. (Ed.), *Stratigraphy & Timescales*. Elsevier. volume 3, pp. 1–80.
- Hinnov, L.A., Park, J., 1998. Detection of Astronomical Cycles in the Stratigraphic Record by Frequency Modulation (FM) Analysis. *J. Sed. Res.* 68, 524–539. doi:[10.2110/jsr.68.524](https://doi.org/10.2110/jsr.68.524).
- Huang, H., Gao, Y., Ma, C., Jones, M.M., Zeeden, C., Ibarra, D.E., Wu, H., Wang, C., 2021. Organic carbon burial is paced by a ~173-ka obliquity cycle in the middle to high latitudes. *Sci. Adv.* 7, eabf9489.
- Husinec, A., Read, J.F., 2023. Milankovitch record from middle Jurassic platform supports moderate coolhouse glaciation. *Paleoceanogr. Paleoclim.* 38, e2023PA004680. doi:[10.1029/2023PA004680](https://doi.org/10.1029/2023PA004680).
- ICS, 2005. Definition and Rank of Quaternary. International Commission on Stratigraphy, <https://stratigraphy.org/files/Q1.pdf>.
- Imbrie, J., Kipp, N.G., 1971. A new micropaleontological method for quantitative paleoclimatology: Application to a late Pleistocene Caribbean core, in: K. K. Turekian (Ed.), *The Late Cenozoic Glacial Ages*. Yale Univ. Press, New Haven, Conn., pp. 71–179.
- Ito, T., Kumazawa, M., Hamano, Y., Matsui, T., Masuda, K., 1993. Long Term Evolution of the Solar Insolation Variation over 4Ga. *Proc. Japan Acad., Series B* 69, 233–237. doi:[10.2183/pjab.69.233](https://doi.org/10.2183/pjab.69.233).
- Ito, T., Masuda, K., Hamano, Y., Matsui, T., 1995. Climate friction: A possible cause for secular drift of Earth’s obliquity. *J. Geophys. Res.* 100, 15147–15162. doi:[10.1029/95JB01061](https://doi.org/10.1029/95JB01061).
- Ito, T., Tanikawa, K., 2002. Long-term integrations and stability of planetary orbits in our Solar system. *MNRAS* 336, 483–500. doi:[10.1046/j.1365-8711.2002.05765.x](https://doi.org/10.1046/j.1365-8711.2002.05765.x).
- Ito, T., Tanikawa, K., 2007. Trends in 20th century Celestial Mechanics. *Pub. Nat. Astron. Observ. Japan* 9, 55–112.
- Javaheri, P., Rein, H., Tamayo, D., 2023. WHFast512: A symplectic N-body integrator for planetary systems optimized with AVX512 instructions. *Open J. Astrophys.* 6. doi:[10.21105/astro.2307.05683](https://doi.org/10.21105/astro.2307.05683).

- Kagan, B.A., Maslova, N.B., 1994. A Stochastic Model of the Earth-Moon Tidal Evolution Accounting for Cyclic Variations of Resonant Properties of the Ocean: An Asymptotic Solution. *Earth, Moon and Planets* 66, 173–188. doi:[10.1007/BF00644130](https://doi.org/10.1007/BF00644130).
- Kent, D.V., Olsen, P.E., Rasmussen, C., Lepre, C., Mundil, R., Irms, R.B., Gehrels, G.E., Giesler, D., Geissman, J.W., Parker, W.G., 2018. Empirical evidence for stability of the 405-kiloyear Jupiter-Venus eccentricity cycle over hundreds of millions of years. *Proc. Nat. Acad. Sci.* 115, 6153–6158. doi:[10.1073/pnas.1800891115](https://doi.org/10.1073/pnas.1800891115).
- Kinoshita, H., 1975. Formulas for Precession. *SAO Special Report* 364.
- Kinoshita, H., 1977. Theory of the Rotation of the Rigid Earth. *Celestial Mechanics* 15, 277–326. doi:[10.1007/BF01228425](https://doi.org/10.1007/BF01228425).
- Kocken, I.J., Zeebe, R.E., 2024. An Astronomically Tuned Time Scale for the Latest Cretaceous (Maastrichtian). *Palaeoceanogr. Palaeoclim.* submitted.
- Kolmogorov, A.N., 1954. On conservation of conditionally periodic motions for a small change in Hamilton's function. *Dokl. Akad. Nauk SSSR* 98, 527–530.
- Lambeck, K., 1980. The Earth's variable rotation: Geophysical causes and consequences. Cambridge University Press, p. 449.
- Lantink, M.L., Davies, J.H.F.L., Hennekam, R., Martin, D.M., Mason, P.R.D., Reichart, G., Hilgen, F.J., 2024. Towards an astrochronological framework for the lower Paleoproterozoic Kuruman and Brockman Iron Formations. *South African J. Geol., Special Issue* doi:doi.org/10.31223/X51H4D.
- Lantink, M.L., Davies, J.H.F.L., Mason, P.R.D., Schaltegger, U., Hilgen, F.J., 2019. Climate control on banded iron formations linked to orbital eccentricity. *Nature Geosci.* 12, 369–374. doi:[10.1038/s41561-019-0332-8](https://doi.org/10.1038/s41561-019-0332-8).
- Lantink, M.L., Davies, J.H.F.L., Ovtcharova, M., Hilgen, F.J., 2022. Milankovitch cycles in banded iron formations constrain the Earth-Moon system 2.46 billion years ago. *Proc. Nat. Acad. Sci.* 119, e2117146119. doi:[10.1073/pnas.2117146119](https://doi.org/10.1073/pnas.2117146119).
- Lantink, M.L., Lenstra, W.K., Davies, J.H.F.L., Hennekam, R., Martin, D.M., Mason, P.R.D., Reichart, G.J., Slomp, C.P., Hilgen, F.J., 2023. Precessional pacing of early Proterozoic redox cycles. *Earth Planet. Sci. Lett.* 610, 118117. doi:[10.1016/j.epsl.2023.118117](https://doi.org/10.1016/j.epsl.2023.118117).
- Laplace, P.S., 1951. A philosophical essay on probabilities; Translated from the 6th French edition by F. W. Truscott and F. L. Emory. Dover Publications, New York.
- Laskar, J., 1985. Accurate methods in general planetary theory. *Astron. Astrophys.* 144, 133–146.
- Laskar, J., 1989. A numerical experiment on the chaotic behaviour of the solar system. *Nature* 338, 237–238. doi:[10.1038/338237a0](https://doi.org/10.1038/338237a0).
- Laskar, J., 1990. The chaotic motion of the solar system - A numerical estimate of the size of the chaotic zones. *Icarus* 88, 266–291. doi:[10.1016/0019-1035\(90\)90084-M](https://doi.org/10.1016/0019-1035(90)90084-M).
- Laskar, J., 2020. Astrochronology, in: Gradstein, F.M., Ogg, J.G., Schmitz, M.D., Ogg, G.M. (Eds.), *Geologic Time Scale 2020*. Elsevier, pp. 139–158. doi:<https://doi.org/10.1016/B978-0-12-824360-2.00004-8>.
- Laskar, J., Fienga, A., Gastineau, M., Manche, H., 2011. La2010: a new orbital solution for the long-term motion of the Earth. *Astron. Astrophys.* 532, A89. doi:[10.1051/0004-6361/201116836](https://doi.org/10.1051/0004-6361/201116836).
- Laskar, J., Joutel, F., Boudin, F., 1993. Orbital, precessional, and insolation quantities from the Earth from -20Myr to +10Myr. *Astron. Astrophys.* 270, 522–533.
- Laskar, J., Robutel, P., Joutel, F., Gastineau, M., Correia, A.C.M., Levrard, B., 2004. A long-term numerical solution for the insolation quantities of the Earth. *Astron. Astrophys.* 428, 261–285, DOI: 10.1051/0004-6361:20041335.
- Lauretano, V., Zachos, J.C., Lourens, L.J., 2018. Orbitally paced carbon and deep-sea temperature changes at the peak of the Early Eocene Climatic Optimum. *Paleoceanogr. Paleoclim.* 33, 1050–1065.
- Laurin, J., Meyers, S.R., Galeotti, S., Lanci, L., 2016. Frequency modulation reveals the phasing of orbital eccentricity during Cretaceous Oceanic Anoxic Event II and the Eocene hyperthermals. *Earth Planet. Sci. Lett.* 442, 143–156. doi:[10.1016/j.epsl.2016.02.047](https://doi.org/10.1016/j.epsl.2016.02.047).
- Laurin, J., Meyers, S.R., Uličný, D., Jarvis, I., Sageman, B.B., 2015. Axial obliquity control on the greenhouse carbon budget through middle- to high-latitude reservoirs. *Paleoceanogr.* 30, 133–149. doi:[10.1002/2014PA002736](https://doi.org/10.1002/2014PA002736).
- Li, M., Hinnov, L., Kump, L., 2019. Acycle: Time-series analysis software for paleoclimate research and education. *Comput. Geosci.* 127, 12–22. doi:[10.1016/j.cageo.2019.02.011](https://doi.org/10.1016/j.cageo.2019.02.011).
- Li, M., Kump, L.R., Hinnov, L.A., Mann, M.E., 2018. Tracking variable sedimentation rates and astronomical forcing in Phanerozoic paleoclimate proxy series with evolutionary correlation coefficients and hypothesis testing. *Earth Planet. Sci. Lett.* 501, 165–179. doi:[10.1016/j.epsl.2018.08.041](https://doi.org/10.1016/j.epsl.2018.08.041).

- Lichtenberg, A.J., Lieberman, M.A., 1983. Regular and Stochastic Motion. Research supported by the U.S. Department of Energy, U.S. Navy, and NSF. New York, Springer-Verlag (Applied Mathematical Sciences. Volume 38), pp. 499.
- Liebrand, D., Beddow, H.M., Lourens, L.J., Pälike, H., Raffi, I., Bohaty, S.M., Hilgen, F.J., Saes, M.J.M., Wilson, P.A., van Dijk, A.E., 2016. Cyclostratigraphy and eccentricity tuning of the early Oligocene through early Miocene (30.1–17.1 Ma): *Cibicides mundulus* stable oxygen and carbon isotope records from Walvis Ridge Site 1264. *Earth Planet. Sci. Lett.* 450, 392–405. doi:[10.1016/j.epsl.2016.06.007](https://doi.org/10.1016/j.epsl.2016.06.007).
- Lieske, J.H., Lederle, T., Fricke, W., Morando, B., 1977. Expressions for the Precession Quantities Based upon the IAU (1976) System of Astronomical Constants. *Astron. Astrophys.* 58, 1–16.
- Liu, H.S., 1995. A new view on the driving mechanism of Milankovitch glaciation cycles. *Earth Planet. Sci. Lett.* 131, 17–26. doi:[10.1016/0012-821X\(95\)00008-Z](https://doi.org/10.1016/0012-821X(95)00008-Z).
- Liu, Y., Huang, C., Ogg, J.G., Algeo, T.J., Kemp, D.B., Shen, W., 2019. Oscillations of global sea-level elevation during the Paleogene correspond to 1.2-Myr amplitude modulation of orbital obliquity cycles. *Earth Planet. Sci. Lett.* 522, 65–78. doi:[10.1016/j.epsl.2019.06.023](https://doi.org/10.1016/j.epsl.2019.06.023).
- Lourens, L.J., 2021. The variation of the Earth’s movements (orbital, tilt, and precession) and climate change, in: Letcher, T.M. (Ed.), *Climate Change*. third ed.. Elsevier, pp. 583–606. doi:<https://doi.org/10.1016/B978-0-12-821575-3.00028-1>.
- Lourens, L.J., Sluijs, A., Kroon, D., Zachos, J.C., Thomas, E., Röhl, U., Bowles, J., Raffi, I., 2005. Astronomical pacing of late Palaeocene to early Eocene global warming events. *Nature* 435, 1083–1087. doi:[10.1038/nature03814](https://doi.org/10.1038/nature03814).
- Ma, C., Meyers, S.R., Sageman, B.B., 2017. Theory of chaotic orbital variations confirmed by Cretaceous geological evidence. *Nature* 542, 468–470. doi:[10.1038/nature21402](https://doi.org/10.1038/nature21402).
- Ma, C., Meyers, S.R., Sageman, B.B., 2019. Testing Late Cretaceous astronomical solutions in a 15 million year astrochronologic record from North America. *Earth Planet. Sci. Lett.* 513, 1–11. doi:[10.1016/j.epsl.2019.01.053](https://doi.org/10.1016/j.epsl.2019.01.053).
- MacDonald, G.J.F., 1964. Tidal Friction. *Rev. Geophys. Space Phys.* 2, 467–541. doi:[10.1029/RG002i003p00467](https://doi.org/10.1029/RG002i003p00467).
- Malinverno, A., Meyers, S.R., 2024. Bayesian Estimation of Past Astronomical Frequencies, Lunar Distance, and Length of Day From Sediment Cycles. *Geochem., Geophys., Geosys.* 25, e2023GC011176. doi:[10.1029/2023GC011176](https://doi.org/10.1029/2023GC011176).
- Meyers, S.R., 2014. Astrochron: An R Package for Astrochronology. cran.r-project.org/web/packages/astrochron/index.html.
- Meyers, S.R., Malinverno, A., 2018. Proterozoic Milankovitch cycles and the history of the solar system. *Proc. Nat. Acad. Sci.* 115, 6363–6368. doi:[10.1073/pnas.1717689115](https://doi.org/10.1073/pnas.1717689115).
- Mignard, F., 1981. The Lunar Orbit Revisited, III. *Moon and Planets* 24, 189–207. doi:[10.1007/BF00910608](https://doi.org/10.1007/BF00910608).
- Milanković, M., 1941. (in German) *Kanon der Erdbestrahlung und seine Anwendung auf das Eiszeitproblem*. Königl. Serb. Akad., pp. 633, Belgrad.
- Minton, D.A., Malhotra, R., 2007. Assessing the Massive Young Sun Hypothesis to Solve the Warm Young Earth Puzzle. *Astrophys. J.* 660, 1700–1706. doi:[10.1086/514331](https://doi.org/10.1086/514331), [arXiv:astro-ph/0612321](https://arxiv.org/abs/astro-ph/0612321).
- Montenari, M., 2018. (Editor) *Stratigraphy & Timescales: Cyclostratigraphy and Astrochronology in 2018*. volume 3. Elsevier.
- Morbidelli, A., 2002. *Modern Celestial Mechanics: Aspects of Solar System Dynamics*. Taylor & Francis, London.
- Morrow, E., Mitrovica, J.X., Forte, A.M., Glisovic, P., Huybers, P., 2012. An enigma in estimates of the Earth’s dynamic ellipticity. *Geophys. J. Internat.* 191, 1129–1134. doi:[10.1111/j.1365-246X.2012.05703.x](https://doi.org/10.1111/j.1365-246X.2012.05703.x).
- Moser, J., 1962. On invariant curves of area-preserving mappings of an annulus. *Nachr. Akad. Wiss. Göttingen*, II , 1–20.
- Motoyama, M., Tsunakawa, H., Takahashi, F., 2020. Tidal resonance of eigenmode oscillation in the early Earth’s ocean and its acceleration effect on the Moon’s orbital evolution. *Icarus* 335, 113382. doi:[10.1016/j.icarus.2019.07.016](https://doi.org/10.1016/j.icarus.2019.07.016).
- Muller, R.A., MacDonald, G.J., 2002. *Ice Ages and Astronomical Causes: Data, Spectral Analysis and Mechanisms*. Environmental Sciences, Springer Berlin, pp. 318.
- Murray, C.D., Dermott, S.F., 1999. *Solar system dynamics*. Cambridge University Press, pp. 592, Cambridge, UK.
- Murray, N., Holman, M., 2001. The role of chaotic resonances in the Solar System. *Nature* 410, 773–779.
- Olsen, P.E., Laskar, J., Kent, D.V., Kinney, S.T., Reynolds, D.J., Sha, J., Whiteside, J.H., 2019. Mapping solar system chaos with the geological orrery. *Proc. Nat. Acad. Sci.* 116, 10664–10673. doi:[10.1073/pnas.1813901116](https://doi.org/10.1073/pnas.1813901116).
- Pälike, H., Laskar, J., Shackleton, N.J., 2004. Geologic constraints on the chaotic diffusion of the solar system. *Geology* 32, 929. doi:[10.1130/G20750.1](https://doi.org/10.1130/G20750.1).

- Piedrahita, V.A., Galeotti, S., Zhao, X., Roberts, A.P., Rohling, E.J., Heslop, D., Florindo, F., Grant, K.M., Rodríguez-Sanz, L., Reghellin, D., Zeebe, R.E., 2022. Orbital phasing of the Paleocene-Eocene Thermal Maximum. *Earth Planet. Sci. Lett.* 598, 117839. doi:[10.1016/j.epsl.2022.117839](https://doi.org/10.1016/j.epsl.2022.117839).
- Poincaré, H., 1914. *Science and Method*; translated by F. Maitland. Nelson & Sons, London.
- Quinn, T.R., Tremaine, S., Duncan, M., 1991. A three million year integration of the earth's orbit. *Astron. J.* 101, 2287–2305. doi:[10.1086/115850](https://doi.org/10.1086/115850).
- Rauch, K.P., Hamilton, D.P., 2002. The HNBODY package for symplectic integration of nearly-Keplerian systems, in: AAS/Division of Dynamical Astronomy Meeting #33, p. 938.
- Rein, H., Liu, S.F., 2012. REBOUND: an open-source multi-purpose N-body code for collisional dynamics. *Astron. Astrophys.* 537, A128. doi:[10.1051/0004-6361/201118085](https://doi.org/10.1051/0004-6361/201118085), [arXiv:1110.4876](https://arxiv.org/abs/1110.4876).
- Rial, J.A., 1999. Pacemaking the Ice Ages by Frequency Modulation of Earth's Orbital Eccentricity. *Science* 285, 564–568. doi:[10.1126/science.285.5427.564](https://doi.org/10.1126/science.285.5427.564).
- Roosbeek, F., Dehant, V., 1998. RDAN97: An Analytical Development of Rigid Earth Nutation Series Using the Torque Approach. *Celest. Mech. Dynamic. Astron.* 70, 215–253. doi:[10.1023/A:1008350710849](https://doi.org/10.1023/A:1008350710849).
- Rozelot, J.P., Damiani, C., 2011. History of solar oblateness measurements and interpretation. *Europ. Phys. J. H* 36, 407–436. doi:[10.1140/epjh/e2011-20017-4](https://doi.org/10.1140/epjh/e2011-20017-4).
- Saha, P., Tremaine, S., 1994. Long-Term Planetary Integration With Individual Time Steps. *Astron. J.* 108, 1962. doi:[10.1086/117210](https://doi.org/10.1086/117210), [arXiv:astro-ph/9403057](https://arxiv.org/abs/astro-ph/9403057).
- Shackleton, N.J., Crowhurst, S.J., Weedon, G.P., Laskar, J., 1999. Astronomical calibration of Oligocene-Miocene time. *Phil. Trans. R. Soc. A* 357, 1907–1929. doi:[10.1098/rsta.1999.0407](https://doi.org/10.1098/rsta.1999.0407).
- Sharaf, S.G., Boudnikova, N.A., 1967. Secular variations of elements of the earth's orbit which influence the climates of the geological past (in russian). *Tr. Inst. Theor. Astron. Leningrad* 11, 233–262.
- Simon, J.L., Bretagnon, P., Chapront, J., Chapront-Touze, M., Francou, G., Laskar, J., 1994. Numerical expressions for precession formulae and mean elements for the Moon and the planets. *Astron. Astrophys.* 282, 663.
- Sørensen, A.L., Nielsen, A.T., Thibault, N., Zhao, Z., Schovsbo, N.H., Dahl, T.W., 2020. Astronomically forced climate change in the late Cambrian. *Earth Planet. Sci. Lett.* 548, 116475. doi:[10.1016/j.epsl.2020.116475](https://doi.org/10.1016/j.epsl.2020.116475).
- Souami, D., Souchay, J., 2012. The solar system's invariable plane. *Astron. Astrophys.* 543, A133. doi:[10.1051/0004-6361/201219011](https://doi.org/10.1051/0004-6361/201219011).
- Spalding, C., Fischer, W.W., Laughlin, G., 2018. An Orbital Window into the Ancient Sun's Mass. *Astrophys. J. Lett.* 869, L19. doi:[10.3847/2041-8213/aaf219](https://doi.org/10.3847/2041-8213/aaf219).
- Standish, E.M., 1998. JPL planetary and lunar ephemerides: DE 405/LE 405. *Jet Propulsion Laboratory Interoffice Memorandum IOM 312.F-98-048*, 1–18.
- Standish, E.M., Newhall, X.X., Williams, J.G., Folkner, W.F., 1995. JPL planetary and lunar ephemerides DE403/LE403. *Jet Propulsion Laboratory Interoffice Memorandum IOM 314.10-127*, 1–27.
- Sussman, G.J., Wisdom, J., 1988. Numerical Evidence that the Motion of Pluto is Chaotic. *Science* 241, 433–437. doi:[10.1126/science.241.4864.433](https://doi.org/10.1126/science.241.4864.433).
- Touma, J., Wisdom, J., 1994. Evolution of the Earth-Moon System. *Astron. J.* 108, 1943. doi:[10.1086/117209](https://doi.org/10.1086/117209).
- Tyler, R.H., 2021. On the Tidal History and Future of the Earth-Moon Orbital System. *Planet. Sci. J.* 2, 70. doi:[10.3847/PSJ/abe53f](https://doi.org/10.3847/PSJ/abe53f).
- van Woerkom, A.J.J., 1953. The Astronomical Theory of Climate Changes, in: Shapley, H. (Ed.), *Climatic Change: Evidence, Causes, and Effects*. Harvard University Press, p. 147.
- Varadi, F., Runnegar, B., Ghil, M., 2003. Successive refinements in long-term integrations of planetary orbits. *Astrophys. J.* 592, 620–630. doi:[10.1086/375560](https://doi.org/10.1086/375560).
- Vervoort, P., Kirtland Turner, S., Rochholz, F., Ridgwell, A., 2024. Earth System Model Analysis of How Astronomical Forcing Is Imprinted Onto the Marine Geological Record: The Role of the Inorganic (Carbonate) Carbon Cycle and Feedbacks. *Paleoceanogr. Paleoclim.* 39, e2023PA004826. doi:[10.1029/2023PA004826](https://doi.org/10.1029/2023PA004826).
- Vondrák, J., Capitaine, N., Wallace, P., 2011. New precession expressions, valid for long time intervals. *Astron. Astrophys.* 534, A22. doi:[10.1051/0004-6361/201117274](https://doi.org/10.1051/0004-6361/201117274).
- Waltham, D., 2015. Milankovitch Period Uncertainties and Their Impact On Cyclostratigraphy. *J. Sediment. Res.* 85, 990–998. doi:[10.2110/jsr.2015.66](https://doi.org/10.2110/jsr.2015.66).

- Ward, W.R., 1974. Climatic variations on Mars: 1. Astronomical theory of insolation. *J. Geophys. Res.* 79, 3375. doi:[10.1029/JC079i024p03375](https://doi.org/10.1029/JC079i024p03375).
- Ward, W.R., 1979. Present obliquity oscillations of Mars: fourth-order accuracy in orbital e and I . *J. Geophys. Res.* 84, 237–241. doi:[10.1029/JB084iB01p00237](https://doi.org/10.1029/JB084iB01p00237).
- Ward, W.R., 1982. Comments on the long-term stability of the Earth's obliquity. *Icarus* 50, 444–448. doi:[10.1016/0019-1035\(82\)90134-8](https://doi.org/10.1016/0019-1035(82)90134-8).
- Webb, D.J., 1982. Tides and the evolution of the earth-moon system. *Geophys. J. R. Astr. Soc.* 70, 261–271. doi:[10.1111/j.1365-246X.1982.tb06404.x](https://doi.org/10.1111/j.1365-246X.1982.tb06404.x).
- Westerhold, T., Marwan, N., Drury, A.J., Liebrand, D., Agnini, C., Anagnostou, E., Barnet, J.S.K., Bohaty, S.M., De Vleeschouwer, D., Florindo, F., Frederichs, T., Hodell, D.A., Holbourn, A.E., Kroon, D., Lauretano, V., Littler, K., Lourens, L.J., Lyle, M., Pälike, H., Röhl, U., Tian, J., Wilkens, R.H., Wilson, P.A., Zachos, J.C., 2020. An astronomically dated record of Earth's climate and its predictability over the last 66 million years. *Science* 369, 1383–1387. doi:[10.1126/science.aba6853](https://doi.org/10.1126/science.aba6853).
- Westerhold, T., Röhl, U., Frederichs, T., Agnini, C., Raffi, I., Zachos, J.C., Wilkens, R.H., 2017. Astronomical calibration of the Ypresian timescale: implications for seafloor spreading rates and the chaotic behavior of the solar system? *Clim. Past* 13, 1129–1152. doi:[10.5194/cp-13-1129-2017](https://doi.org/10.5194/cp-13-1129-2017).
- Westerhold, T., Röhl, U., Raffi, I., Fornaciari, E., Monechi, S., Reale, V., Bowles, J., Evans, H.F., 2008. Astronomical calibration of the paleocene time. *Palaeogeogr. Palaeoclim. Palaeoecol.* 257, 377–403.
- Williams, J.G., 1994. Contribution to the Earth's Obliquity Rate, Precession, and Nutation. *Astron. J.* 108, 711. doi:[10.1086/117108](https://doi.org/10.1086/117108).
- Wu, H., Hinnov, L.A., Zhang, S., Jiang, G., Yang, T., Li, H., Xi, D., Ma, X., Wang, C., 2023. Continental geological evidence for Solar System chaotic behavior in the Late Cretaceous. *Geol. Soc. Am. Bull.* 135, 712–724. doi:[10.1130/B36340.1](https://doi.org/10.1130/B36340.1).
- Wu, H., Zhang, S., Jiang, G., Hinnov, L., Yang, T., Li, H., Wan, X., Wang, C., 2013. Astrochronology of the Early Turonian–Early Campanian terrestrial succession in the Songliao Basin, northeastern China and its implication for long-period behavior of the Solar System. *Palaeogeogr. Palaeoclim. Palaeoecol.* 385, 55–70. doi:[10.1016/j.palaeo.2012.09.004](https://doi.org/10.1016/j.palaeo.2012.09.004).
- Wu, Y., Malinverno, A., Meyers, S.R., Hinnov, L.A., 2024. A 650-Myr history of Earth's axial precession frequency and the evolution of the Earth-Moon system derived from cyclostratigraphy. *Sci. Adv.* in press.
- Zachos, J.C., Pagani, M., Sloan, L., Thomas, E., Billups, K., 2001. Trends, rhythms, and aberrations in global climate 65 Ma to present. *Science* 292, 686–693.
- Zeebe, R.E., 2015. Dynamic stability of the Solar System: Statistically inconclusive results from ensemble integrations. *Astrophys. J.* 798, 8. doi:[10.1088/0004-637X/798/1/8](https://doi.org/10.1088/0004-637X/798/1/8).
- Zeebe, R.E., 2015. Highly stable evolution of Earth's future orbit despite chaotic behavior of the Solar System. *Astrophys. J.* 811, 9. doi:[10.1088/0004-637X/811/1/9](https://doi.org/10.1088/0004-637X/811/1/9).
- Zeebe, R.E., 2017. Numerical Solutions for the Orbital Motion of the Solar System over the Past 100 Myr: Limits and New Results. *Astron. J.* 154, 193. doi:[10.3847/1538-3881/aa8cce](https://doi.org/10.3847/1538-3881/aa8cce).
- Zeebe, R.E., 2022. Reduced variations in Earth's and Mars' orbital inclination and Earth's obliquity from 58 to 48 Myr ago due to solar system chaos. *Astron. J.* 164, 107. doi:[10.3847/1538-3881/ac80f8](https://doi.org/10.3847/1538-3881/ac80f8).
- Zeebe, R.E., 2023. OrbitN: A Symplectic Integrator for Planetary Systems Dominated by a Central Mass – Insight into Long-term Solar System Chaos. *Astron. J.* 166. doi:[10.3847/1538-3881/acd63b](https://doi.org/10.3847/1538-3881/acd63b), [arXiv:2306.03737](https://arxiv.org/abs/2306.03737).
- Zeebe, R.E., Lantink, M.L., 2024a. A secular solar system resonance that disrupts the dominant cycle in Earth's orbital eccentricity (g_2-g_5): Implications for astrochronology. *Astron. J.* 167, 204. doi:doi.org/10.3847/1538-3881/ad32cf.
- Zeebe, R.E., Lantink, M.L., 2024b. Milanković Forcing in Deep Time. *Paleoceanography and Paleoclimatology* 39.
- Zeebe, R.E., Lourens, L.J., 2019. Solar system chaos and the Paleocene-Eocene boundary age constrained by geology and astronomy. *Science* 365, 926–929.
- Zeebe, R.E., Lourens, L.J., 2022a. A deep-time dating tool for paleo-applications utilizing obliquity and precession cycles: The role of dynamical ellipticity and tidal dissipation. *Paleoceanogr. Paleoclim.* 37, 2021PA004349. doi:[10.1029/2021PA004349](https://doi.org/10.1029/2021PA004349).
- Zeebe, R.E., Lourens, L.J., 2022b. Geologically constrained astronomical solutions for the Cenozoic era. *Earth Planet. Sci. Lett.* 592, 117595. doi:[10.1016/j.epsl.2022.117595](https://doi.org/10.1016/j.epsl.2022.117595).
- Zeeden, C., Meyers, S.R., Lourens, L.J., Hilgen, F.J., 2015. Testing astronomically tuned age models. *Paleoceanogr.* 30, 369–383. doi:[10.1002/2014PA002762](https://doi.org/10.1002/2014PA002762).
- Zhang, S., Wang, X., Hammarlund, E.U., Wang, H., Mafalda Costa, M., Bjerrum, C.J., Connelly, J.N., Zhang, B., Bian, L., Canfield, D.E., 2015. Orbital forcing of climate 1.4 billion years ago. *Proc. Nat. Acad. Sci.* 112, E1406–E1413. doi:[10.1073/pnas.1502239112](https://doi.org/10.1073/pnas.1502239112).